Oceanic heat transport towards the Getz Ice Shelf, Amundsen Sea

Master's thesis in
Physical Oceanography

Vår Dundas

GEOPHYSICAL INSTITUTE

20 November 2019

The ice shelf in the photograph
on the front page is the Getz Ice Shelf,
captured by Povl Abrahamsen, BAS.

Acknowledgements

I want to thank Elin Darelius for valuable feedback and guidance, and for letting me tag along to FRISP (and for keeping me on track when the SAM is suddenly the most fascinating driver of variability in the Amundsen Sea), Kjersti Daae for focusing on the details and for encouraging remarks, and to Nadine Steiger for always having time to read my first drafts and for helpful discussions.

Thanks to Karen Assmann for taking the time to discuss my results, for feedback and for sharing useful model results, to KOPRI for making CTD-data available and for assistance with mooring deployment/recovery, to Yixi Zheng for telling me about the seal and to Louise Briddle for providing the data set, and all motivating discussions at FRISP.

And finally, thanks to Lise for sharing breakdowns and breakthroughs these last months at our tiny study hall, to GFI for five amazing years, and to Håkon, who probably knows just as much about the Amundsen Sea as I do by now, thanks to my continuous talk about this thesis.

Abstract

The highest rates of ice shelf melt in Antarctica are found in West Antarctica. This is mainly due to the presence of warm Circumpolar Deep Water on the continental shelf, where it may come in direct contact with the ice shelves. Two years of mooring data (UIB3: 2016-2018) from a trough (the UIB3-trough) leading up to one of the central ice shelf fronts of the Getz Ice Shelf, Western Amundsen Sea, are used to describe the local hydrography and currents, their variability and possible drivers of this variability. Relatively warm modified Circumpolar Deep Water is present throughout the mooring period (maximum temperature: 0.13°C), but meltwater is not observed. The mean current at UIB3 is weak (0.03m/s), and is directed towards the ice shelf. We discuss the observed variability in heat content in relation to interannual effects of changes in ocean surface stress. To study mechanisms that may bring modified Circumpolar Deep Water to UIB3, we investigate the impact of the ocean surface stress on the Ekman pumping at the shelf break, and discuss its relative importance in relation to variability in the along-slope eastward undercurrent, and the strength of the Antarctic Slope Front. The heat transport is closely connected to the current towards the ice shelf at UIB3. This current, and the ocean surface stress, have significant correlation that shifts between positive and negative values, in periods that tend to follow the seasons. Having only two years of mooring data limits us from drawing conclusions on the seasonality in our results. The highest correlation of about 0.5, with ∼15h lag, is found between the along-slope current at UIB3, and the ocean surface stress from a region east of UIB3, at the location of the Amundsen Sea Polynya. The observed seasonal signal in the westwards coastal current may be of importance for this high correlation, since it passes through the polynya and continues past regions near UIB3. We estimate that the upper limit of ice melt caused by the heat transport in the UIB3-trough may contribute to roughly 0.6m/year of the total ice melt of the Getz Ice Shelf.

Acronyms

ACC	Antarctic Circumpolar Current
ASF	Antarctic Slope Front
ASL	Amundsen Sea Low
CDW	Circumpolar Deep Water
mCDW	modified Circumpolar Deep Water
SAM	Southern Annular Mode
SB-box	Shelf Break box
SIC	Sea ice concentration
S16	Summer 2016
S17	Summer 2017
W16	Winter 2016
W17	Winter 2017
WW	Winter Water

C	Correlation coefficient
C_p	Threshold correlation value
DOF	Degree of freedom
H	Areal density of heat
N	Number of windows with significant correlation
Q	Transport density of heat
r	Significant correlation
τ_{no-ice}	Ocean surface stress without inclusion of sea ice
τ_{Cd}	Ocean surface stress following Andreas et al. (2010)
τ_{ERA5}	Ocean surface stress provided by ERA 5
τ_{ice}	Ocean surface stress following Dotto et al. (2018)
w_{EK}	Vertical Ekman pumping velocity

Contents

Chapter 1

Introduction

Antarctica's ice shelves are melting at an accelerating rate (Rignot et al., 2019), mainly due to high ocean temperatures (e.g. Pritchard et al., 2012). When the ice sheets melt, their buttressing effects on the continental glaciers decrease, and previously grounded ice may become part of the floating ice shelves (e.g. Dupont and Alley, 2005). The immense volume of grounded ice means that melting of this ice has the potential to induce a wide range of global changes, from changes in the gravitational field, the earths rotation, induce effects of isostatic adjustment, and of course, sea level rise. For the latter, the ice does not have to melt, it simply needs to become ungrounded. Following the IPCC's RCP 8.5 scenario, ice melt in Antarctica might contribute to more than 15 meters of the global sea level rise by 2500 (DeConto and Pollard, 2016).

The highest rates and acceleration of ice shelf melt in Antarctica are found in West Antarctica (Fig. 1.1, Shepherd et al., 2018; Rignot et al., 2013; Pritchard et al., 2012), and it is estimated that about 10% of today's observed global sea level rise is the result of melting in this region (Jenkins et al., 2010). The explanation for these changing and high melt rates lies in the on-shelf presence of Circumpolar Deep Water (CDW), which has a core temperature of about 2°C (Heywood et al., 2016). Whereas many regions in Antarctica loose most glacial mass through calving, the proximity of CDW means that the high melt rates is the main reason for mass loss in West Antarctica (Rignot et al., 2013). When CDW, or colder, modified versions (mCDW), come in direct contact with an ice shelf, melting will occur. In the Eastern Amundsen Sea, an increase in meltwater production of 50% has been observed between 1994 and 2009 (Jacobs et al., 2011). The characteristics of the bathymetry has proven to be crucial when distinguishing between areas of high and low melt rates, as glacially scoured troughs act like channels that lead the dense and warm CDW from the shelf break, onto the continental shelf, and towards the ice shelves (e.g. Jacobs et al., 2011). In parallel to the high melt rates, the sea ice season has been found to be about two months shorter today than it was in 1979, reflecting changes in large scale

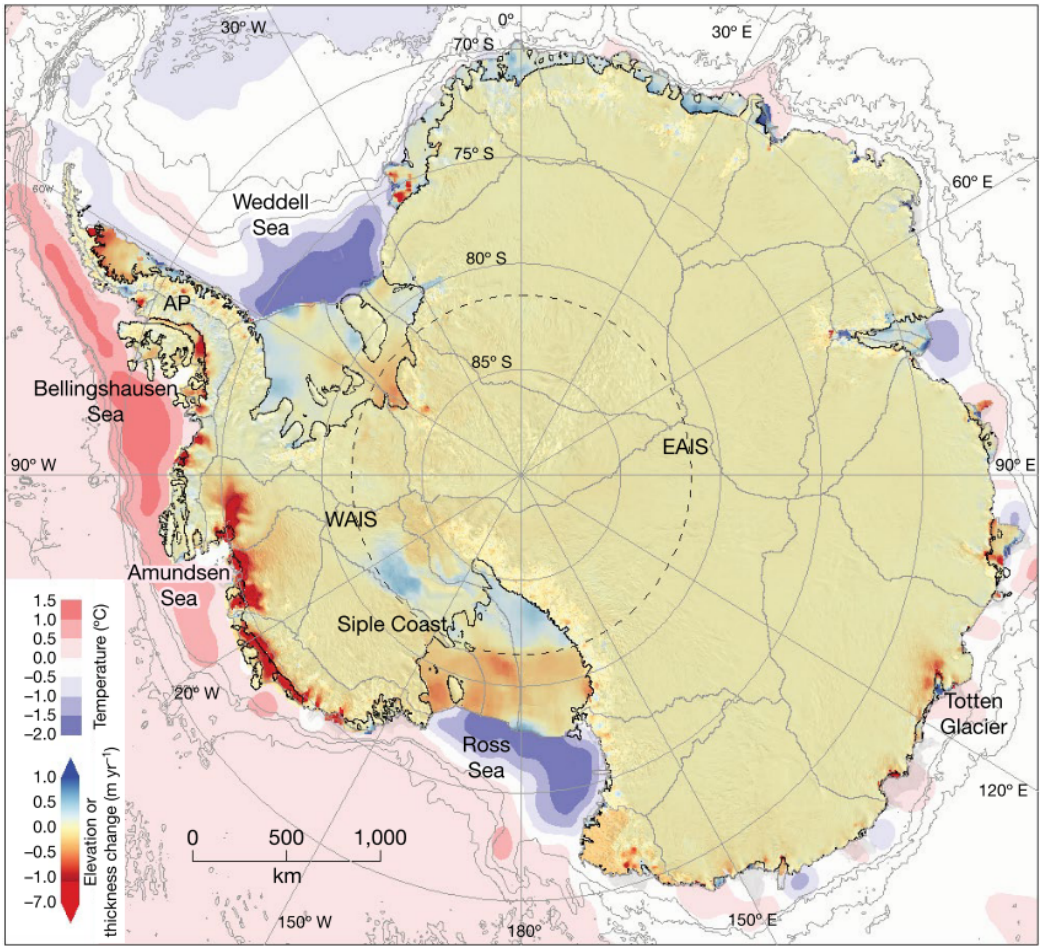

Figure 1.1: The rate of change in ice-shelf thickness (1992-2017), and estimated temperature at the sea-floor throughout Antarctica (Shepherd et al., 2018)

systems over Western Antarctica (Yager et al., 2012).

Due to these large and accelerating changes, this region has received increased attention over the last two decades. Four moorings from the University of Bergen (UiB) were deployed between 2016 and 2018 in the Western Amundsen Sea, near the Getz Ice Shelf between 2016 and 2018 (Fig. 2.1 and 3.1), where melt rates are estimated to approach 5 meters per year (Rignot et al., 2013). As research on ocean circulation and ice melt in the Amundsen Sea has a short history, with the first available hydrographic observations measured in 1994 (Jacobs et al., 2012; Heywood et al., 2016), these four moorings and associated CTD stations provide a large contribution to the knowledge in the area. We studied the data from one of these moorings, UIB3 (Fig. 2.1), in detail. UIB3 was located in a trough in front of the middle of the Getz Ice Shelf. While regions both to the west (e.g. Assmann et al., 2019)

and east (e.g. Wåhlin et al., 2010), have previously been studied in some detail, the region of UIB3 is mainly unexplored, and at the boundary of regional models (e.g. Dotto et al., 2019; Assmann et al., 2013; Arrigo, 2003).

The aim of this study is to give an overview of the hydrography and the observed currents at the mooring-site during these two years, to describe their variability and to investigate possible drivers. Due to the high melt rates in the overall Amundsen Sea region, we especially focus on variability in heat content and thickness of the warm layer, as well as the heat transport towards the ice shelf. Previous studies have found shelf break processes driven by the wind field and ocean surface stress to be crucial for the flow of CDW onto the continental shelf (e.g. Assmann et al., 2019; Dotto et al., 2019), and we therefore investigate correlation between the ocean surface stress and both heat content, and the observed along-flow velocity past UIB3.

The shelf break north of UIB3 is relatively shallow compared to areas with particularly high melt rates, which means that the warm water off-shelf needs to be lifted higher up in order to flow onto the continental shelf. We do, however, find evidence of mCDW at the mooring site. We can therefore use data from UIB3 to investigate which processes can be responsible for the variability in heat content in areas without deep troughs cutting into the shelf break. We further discuss possible pathways of mCDW towards the mooring site. We pay special attention to the interannual variability and the seasonal differences, and attempt to connect the observed large-scale characteristics in the ocean surface stress and Ekman pumping to the local variability at the mooring-site. Results from previous studies (e.g. Dotto et al., 2019; Jacobs et al., 2013; Assmann et al., 2019), numerical model simulations (Assmann et al., 2013; Nakayama et al., 2014), and historical CTD-profiles, enables us to compare the observations from 2016-2018 with the general situation at the mooring-site, although the data basis is still not extensive enough to draw definite conclusions. Finally, we comment on limitations of this study and include an outlook for future studies.

Chapter 2

Background: Oceanographic Setting and Theory

In this section we introduce the oceanographic setting needed to get a general understanding of the study region. Since we study both local variability at the mooring site of UIB3, and possible drivers of this variability, we go into some detail about both the local characteristics of the mooring area, and the large scale systems influencing the entire Amundsen Sea. We address the topics in the following order:

- Local geography, mean wind field, currents, and sea ice cover,
- Circumpolar Deep Water,
- The Antarctic Slope Front and the along-slope undercurrent,
- The Amundsen Sea Low and the Southern Annual Mode,
- Theory behind calculation of heat content and heat transport, Ekman pumping velocity and ocean surface stress, and
- Theoretical aspects of correlation, spectral analysis and signal filtering.

2.1 The Western Amundsen Sea

Geography

The Western Amundsen Sea lies between the Ross Sea and the Antarctic Peninsula (Fig. 2.1). The bathymetry is characterized by troughs cutting into the continental shelf, and

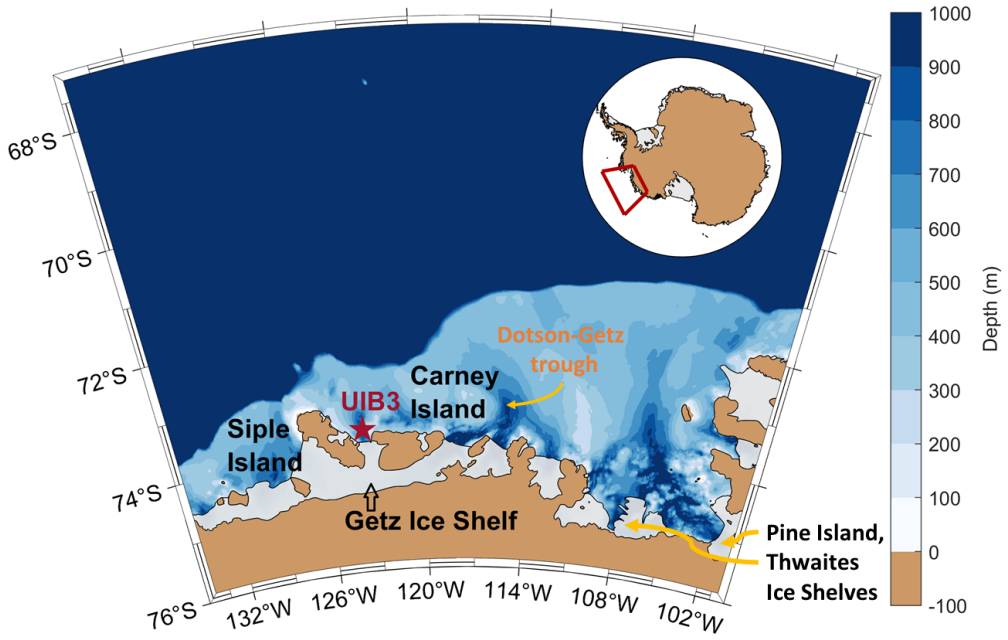

Figure 2.1: Map showing the location of UIB3 (red star) between Siple and Carney Island in the Amundsen Sea. The color scale indicates the bathymetry (IBCSO), and the inset shows the location of the study area on the Antarctic continent (red square). Fig. 3.1 show the mooring location in more detail.

large differences in the broadness of the shelf. UIB3 was located in the trough between Siple and Carney Islands, about 30 km from the ice shelf, and about 130 km from the continental shelf break. We refer to this trough as the UIB3-trough hereafter. Towards the east the continental shelf broadens to the north over a relatively short distance, creating a sharp bend in the shelf break bathymetry. The southern part of the UIB3-trough is about 1000 m deep, while the northern part is around 800 m deep (Lee, 2016). The trough does not extend all the way north to the continental shelf break, where the shelf break is approximately 460 m deep. This distinguishes it from other troughs in the Amundsen Sea where CDW flows onto the shelf, such as the Siple trough west of Siple Island, where the shelf break is about 570 m deep, and extends all the way from shelf break in the north to ice shelf in the south.

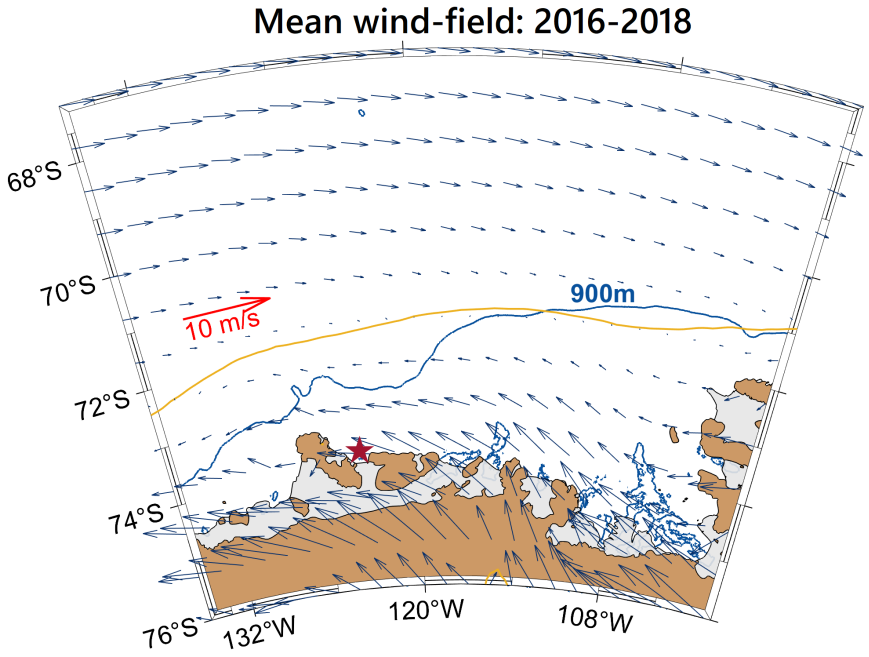

Figure 2.2: The mean wind-field (arrows) from ERA 5 (ECMWF, 2018) during the mooring period (2016-2018). The zero-contour (yellow line), the 900 m isobath (blue line), the mooring location (red star), and a red arrow for scale is included.

The wind field

All around Antarctica, katabatic winds with a strong northwards component flow off the continent, and bend towards the west due to the Coriolis force. This leads to relatively zonal westward winds that flow over the continental shelf in a band around 74°S. North of the continental shelf around 70°S, the winds are zonal in the eastward direction (e.g. Spence et al., 2014). Apart from the katabatic winds from the continent, meridional components are generally weak. The strength of the zonal winds and the latitude of the zero-contour, i.e. where the zonal wind changes direction, vary seasonally (Assmann et al., 2013), and along the Antarctic coast. Both the strength of these winds, and the location of the zero-contour are features that are important for other characteristics, such as the Ekman pumping (section 2.5.2), the Antarctic Slope Front (section 2.3) and the along-slope undercurrent (section 2.3). The mean wind field over the mooring period is shown in Fig. 2.2.

The position of the zero-contour is influenced by large-scale atmospheric systems such as the Southern Annual Mode and the Amundsen Sea Low (section 2.4, and e.g. Raphael et al.,

2016; Stammerjohn et al., 2015; Thompson and Solomon, 2002). The seasonal changes in the mean latitude of the zero-contour is described by Assmann et al. (2013) over the period 1979-2011. During summer, it shifts north, and is at its most extreme in January at about 69°S. During winter it shifts south, and lies around 72°S in August. It changes position faster during the summer months, and stays in the southern half of the latitude-range for more than half of the year.

Currents

The currents in this region have not been widely studied, but we have obtained the mean current field for 2011-2012, from a numerical model study (Assmann et al., 2013), and selected depths of 15 m, 225 m 450 m, and 525 m to get a general impression of the mean state of the currents in the region (Fig. 2.3). The closest model boundary is the western boundary at 139°W, so we do not expect boundary effects.

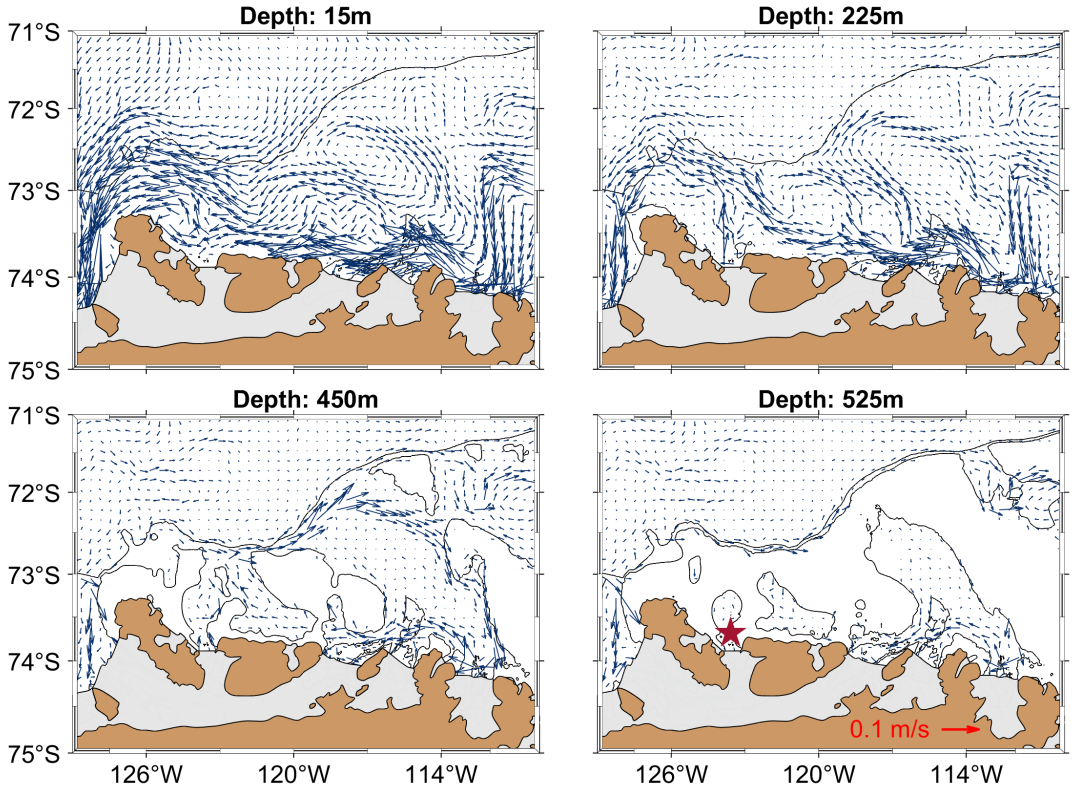

Figure 2.3: Mean (2011-2012) currents at 15m, 225m, 450m, and 525m depth according to a numerical model study (Assmann et al., 2013). The scale indicated by the red arrow in the lower right panel is valid for all panels. The mooring location is indicated by the red star.

In the surface layer, at 15 m depth, the westward coastal current is dominant, and there is evidence of a westward current along the continental shelf break. The coastal current is geostrophic, and is driven by the coastal easterlies that induce southward Ekman transport and a meridional gradient in sea surface height (SSH), with higher SSH furthest south along the coastline (Dotto et al., 2018). A cyclonic circulation system appear in the general location of the Dotson-Getz trough, around 117°W, 72.5°S. At 225 m depth, within the layer of winter water (WW), (e.g. Jacobs et al., 2013), the coastal current is still strong, but bends north-westwards before reaching the UIB3-trough. The westwards current at the shelf break does not extend this deep, but the cyclonic circulation in the Dotson-Getz trough can be distinguished. At 450 m depth, which is the horizontal layer closest to 460m in the model i.e. the shelf break depth north of UIB3, currents are much weaker, but we still see evidence of the westward coastal current. At the shelf break, the eastward undercurrent is apparent (section 2.3). It turns onto the shelf at about 117°W, where it veers south. Once it reaches the coast, it connects with the coastal current. At this depth, the current is cut off from UIB3 by bathymetry, although we note that the bathymetry is uncertain (section 3.2.1). These currents agree relatively well with the bottom currents from a model run by Nakayama et al. (2014) over the period 1984-1998. The next horizontal layer in the model is 520 m depth. Here the UIB3-trough is cut off from waters north of the shelf break, and currents are in general weak.

The tidal currents in the region are also generally weak (Padman et al., 2018), apart from two patches of stronger currents north of Siple Island and along the shelf break between about 114°W and 118°W (not shown). These patches appear in the K1, O1 and M2 constituents in the tidal model CATS2008 which is an update to the model described by Padman et al. (2002).

Sea ice

The mean sea ice extent exhibit a large variability throughout the year, though averaged over 1979-2012, the continental shelf break is always covered with a certain percentage of sea ice (Stammerjohn et al., 2015). The smallest extent is found in February, when open water is found at about 70°S, whereas in winter, the mean maximum extent is at about 65°S. During summer, the sea ice concentration (SIC) also decrease, and large polynyas, such as the Amundsen Sea Polyna, which has its maximum extent in January (Arrigo, 2003), expand along the coast. In contrast, SIC is nearly 100% over large areas during winter. This variation in SIC and extent means that the interaction between the atmosphere and the ocean is more direct in the region of the continental shelf break during summer. Aspects of interactions between wind stress and sea ice, and the resulting ocean surface stress, is considered in section 2.5.3.

Possibly due to interactions between the topography of Carney Island and the northwestward mean winds (Fig. 2.2), a polynya tends to form on the western side of Carney Island. The westward coastal currents also transport sea ice past Carney Island and into the polynya. The winds thus periodically open and close the polynya (K. Assmann, personal communication).

2.2 Circumpolar Deep Water

Circumpolar Deep Water (CDW) is a relatively warm and saline fraction of the eastward-flowing Antarctic Circumpolar Current (ACC), and is found all around Antarctica. Unmodified CDW has a conservative temperature larger than 1°C and an absolute salinity larger than 34.85g/kg (e.g. Assmann et al., 2019), but temperatures as high as 2°C have been observed (e.g. Heywood et al., 2016). The density of the CDW is high due to the high salinity that exceeds the opposite effect of its high temperature which means that it, in general, is found at depths greater than the continental shelf (Heywood et al., 2016), and therefore does not have direct access onto the shelf.

The Antarctic Slope Front (ASF) separates the cold, overlying Winter Water (WW) from the warm CDW at the shelf break (Fig. 2.4). This front is present where the isotherms in the thermocline between WW and CDW slope down towards the continental shelf break (e.g. Jacobs, 1991; Heywood et al., 2016; Spence et al., 2014), and act like a boundary, blocking properties on the continental shelf from interacting with properties in the deep ocean. We further describe the ASF and its associated system of slope currents in section 2.3. Although CDW may occasionally reach depths above the local shelf break depth, the ASF tends to impede the inflow of CDW. CDW do not normally have access to the shelf areas, however, branches of this warm, dense water occasionally find its way onto the continental shelf (Fig 2.4).

In the Amundsen Sea, channels, or troughs, cut into the shelf (Jacobs et al., 2012). These troughs were made by glacial processes, and are now under-water u-shaped valleys, which are usually at their deepest near their respective ice shelves (Fig. 2.1). However, in some places the troughs extend all the way to the shelf break (Fig. 2.1), leading to a particularly deep shelf break in front of the trough. This may leave a gap between the ASF and the deep shelf break (Fig. 2.4), which allows CDW to flow onto the shelf, along the trough, below the WW. The warmest and densest CDW find its way onto the shelf through such troughs in the shelf break at mainly $120°W$, $114°W$, $118°W$ and $128°W$ that (Thoma et al., 2008). The consequence is particularly large melt rates and loss of ice mass in the Amundsen Sea region (Rignot et al., 2008; Pritchard et al., 2012).

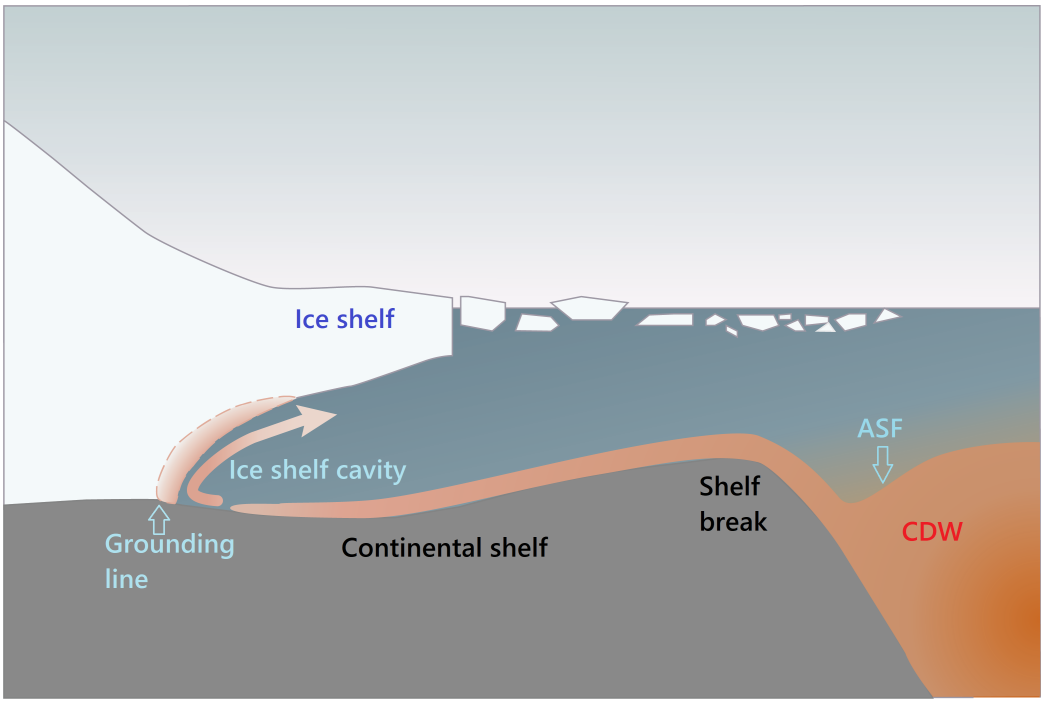

Figure 2.4: Schematic showing how Circumpolar Deep Water flows onto the continental shelf and reaches the grounding line to cause melting. Credit: Kjersti Daae.

The width of the continental shelf in the Amundsen Sea is highly variable (Fig. 2.1), stretching over $\sim$ 550km at the most at the eastern end towards Pine Island and Thwaites Glacier (Fig. 2.1), and only over $\sim$ 160km in the western parts towards the Getz Ice Shelf. When the CDW reaches the ice shelves, the temperature is reduced by about 0.5°C in the east, due to mixing at the shelf break (Heywood 2016), while it is unmodified in the west (Assmann et al., 2019). Despite the lower temperatures in the Eastern Amundsen Sea, this is where the highest melt rates are found (Rignot et al., 2008).

Ocean heat and related ice shelf basal melt

One of the largest concerns in relation to the presence of CDW on the continental shelf is the possibility that warm water may reach the grounding lines of the ice shelves. The grounding line is where the ice sheet is no longer connected to the bedrock, but transitions into a floating ice shelf (Fig 2.4). In the Amundsen Sea, the CDW is denser than the shelf-water, and inflow of CDW occur near the bottom (Fig. 2.4). This means that when CDW flows onto the shelf, the high density means that if it flows far enough south, and if the layer of warm water is thick enough, it will likely cause ice melt. In the case of the Getz Ice Shelf, the grounding lines are found at depths of several hundred meters, which means

that the pressure here is much higher than at the surface. The freezing point of salt water decreases as a function of pressure, so while the freezing point at surface pressure is -1.9°C at a salinity of ~ 35 psu, the freezing point at e.g. 2km depth is about -3.4°C (Fig. 2.5, and Holland, 2013).

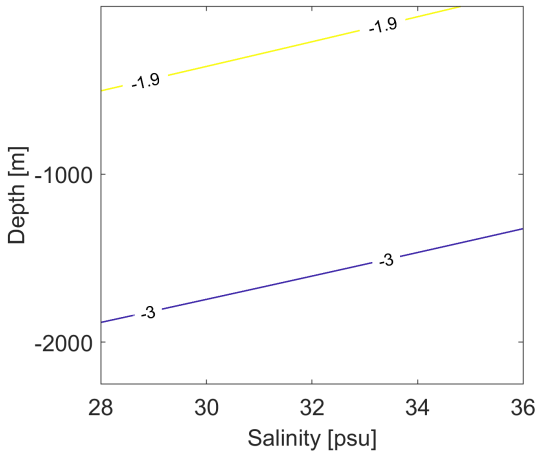

Figure 2.5: The freezing point of seawater (yellow and blue contour) is dependent on both salinity and depth. When salinity and depth increase, the freezing point decreases.

A water mass at surface freezing point therefore has the potential to melt the ice shelf at greater depths because of the decrease in freezing point. To circumvent this issue in calculations, it is common to look at profiles of $T - T_f$, where T_f is the in situ freezing temperature, instead of the measured temperature, as this adjusts for the large pressure differences between the surface and the grounding lines.

Gade (1979) provides a method for investigating whether or not meltwater is present when studying water masses in a TS-diagram. If the data points in T-S space align with the Gade-line, it indicates that meltwater is present (Fig. 4.2). We evaluate the line following Gade (1979):

$$T_p(S_p) = T_{ocean} + \frac{L_f}{C_p}\left(1 - \frac{S_{ocean}}{S_p}\right) \tag{2.1}$$

using $T_{ocean} = -0.4$°C, $S_{ocean} = 34.4$°C, $L_f = 334$ kJ/kg and $C_p = 3.97$ kJ/kg K. T_p and S_p is the resulting temperature and salinity of the meltwater mixture when we assume that the temperature of the ice is warmer than -30°C, and that the volume of meltwater is small relative to the ocean volume. When these requirements are met, the energy needed for warming the ice and warming the resulting meltwater is negligible compared to the energy needed for melting the ice, i.e. the required sensible heat transfer (related to C_p) is small relative to the required latent heat transfer (related to L_f) (Gade, 1979).

2.3 Antarctic Slope Front and the along-slope undercurrent

Two currents are associated with the ASF - one westward surface current, and one deeper eastwards undercurrent. We describe the dynamics related to the characteristics of the ASF and these two currents in this section. The ASF is generally not seen at the surface, but at depth it keeps waters on-shelf and off-shelf separated, and is identified by meridional temperature gradients (Fig. 2.4, and Jacobs, 1991). The presence of the ASF in the Amundsen Sea is not clear: Spence et al. (2014) and Jacobs (1991) state that the ASF extends from the Amundsen Sea region and westwards all the way to the Antarctic Peninsula, while Stewart and Thompson (2015) state that the ASF is not present in the Bellingshausen Sea nor the Amundsen Sea. As the literature does not agree on the presence of the ASF in the shelf break region north of UIB3, it is important to be familiar with mechanisms that influence the ASF since it is connected to the potential inflow of warm waters onto the shelf.

Ekman pumping is important for the characteristics of the ASF. Strong easterlies lead to Ekman transport towards the coast, which in turn leads to convergence and downward Ekman pumping. The coastal downwelling pushes the isopycnals down so that relatively fresh and cold surface waters on the continental shelf is separated from off-shelf waters such as the CDW (Spence et al., 2014). When strong gradients in the ocean surface stress sets up a sharp slope front, it drives a westward surface current, and an eastward undercurrent along the shelf break (Fig 2.3) through geostrophy (Walker et al., 2013). If the winds decrease in strength, the ASF relaxes, and the slope-currents slow down. The summertime situation of strong easterlies are important to set up this slope-current system, but when the westerlies shift southwards in the winter, it has been suggested that eastward flowing currents over the whole depth is likely (Assmann et al., 2013). The latitude of the zero-contour also influences the strength of the ASF (Stewart and Thompson, 2015; Spence et al., 2014), because a southward shift in the zero-contour is connected to a weaker SSH gradient towards the coast due to suppressed coastal easterlies and weaker coastal downwelling (Spence et al., 2014), and a change in the location of upwelling due to divergence in the wind field (section 2.5.2). Where the continental slope is steep, the ASF tends to be sharp (Stewart and Thompson, 2015).

The along-slope eastward undercurrent, induced by a sharp slope front, plays an important role in bringing CDW onto the continental shelf in certain areas in the central and Eastern Amundsen Sea (e.g. Dotto et al., 2019). The variability of the undercurrent has been found to be high over short distances (Walker et al., 2013), so it is unfortunate that we lack information about the characteristics of the current at the shelf break north of UIB3 during the mooring-period. However, both the numerical model-average over 2011-2012 (Fig. 2.3, and Assmann et al., 2013) and the model average over 1989-1998 by Nakayama et al. (2014), indicate that the undercurrent is generally present at the shelf break north of UIB3.

2.4 The Amundsen Sea Low and Southern Annular Mode

To end this description of the oceanographic setting, we mention two large-scale atmospheric features that influence the general conditions in the Amundsen Sea: the Amundsen Sea Low (ASL) and the Southern Annular Mode (SAM).

The Amundsen Sea Low represents a large cyclonic circulation system, which on average shift between eastern regions to the north near the Antarctic Peninsula in summer, and western regions to the south towards the Ross Sea in winter (Raphael et al., 2016). This means that this cyclonic system passes over the Amundsen Sea twice a year, influencing the gradients in the wind field. A strengthening of the ASL has been observed in recent years, which has been connected to changes in ocean circulation and surface temperature (Raphael et al., 2016).

The SAM, also called the Antarctic Oscillation, describes how the mean westerlies in the Southern Ocean periodically shift northward and southward, and is forced by meridional differences in sea level pressure between mid-latitudes and high latitudes (Thompson et al., 2011). The SAM-index is defined as the difference in zonal mean sea level pressure (SLP) between 40°S, and 65°S (Gong and Wang, 1999), and adjusted so that the historical (1979-2000) mean and standard deviation is respectively zero and one (NOAA, 2019). When SAM is positive, the westerlies are shifted south, while in its negative mode the westerlies shift northwards (Thompson et al., 2011). In the positive mode, the winds also increase in intensity. A general result of the southward shift of the midlatitude westerlies is that the coastal easterly winds are suppressed and weaken, leading to a decrease in Ekman pumping intensity, and consequently a relaxed ASF (Spence et al., 2014). The spatial coverage of sea ice also tends to increase when SAM is positive (Lefebvre and Goosse, 2005).

Although the SAM has a circumpolar signature, it is particularly influential in the Southern Pacific (Fyfe and Saenko, 2006; Gong and Wang, 1999). In recent years, a positive trend of the SAM-index has been observed and is associated with increased anthropogenic CO^2 emissions and ozone depletion (e.g. Thompson and Solomon, 2002; McLandress et al., 2011). Fyfe and Saenko (2006) estimate that the zonal wind stress in the Pacific sector will increase by 40%, and shift southward by 3.5° by the end of this century. However, the models used in this study indicate present-day values that are too low and too far north (Fyfe and Saenko, 2006), so it is possible that the future values should be even higher than the models predict, or that the models do not correctly represent the dynamics that determines the position of the westerlies.

2.5 Theory

We need to evaluate a couple of central variables to describe the variability and its drivers in this region. Due to the high temperatures of mCDW, variables such as heat content and heat transport past UIB3 are relevant. In relation to the ASF, we study the Ekman pumping to investigate the potential for lifting of the isopycnals at the continental shelf break. The Ekman pumping is in turn dependant on the ocean surface stress, which we estimate in relation to sea ice concentration. In this section we look into the theory and calculation of these properties.

2.5.1 Heat content and heat transport

By definition, heat content is a measure of the amount of energy within a system, and is measured in Joules. It is dependent on the specific heat, c_p, and density, ρ, of the fluid, and in our case we regard these as constants. Ideally we would calculate the heat content for a volume of the ocean, but temperature measurements are only available along one axis. We therefore calculate the areal density of heat, H:

$$H = \rho c_p \int_{z_0}^{z_1} T(z) dz \tag{2.2}$$

where ρ is 1028 kg m^{-3} and c_p is 3985 J kg^{-1} K^{-1}. z_0 and z_1 is the bottom and top of the mooring, and $T(z)$ is the temperature. The unit of H is J/m^2.

Heat transport has the unit J m/s , but analogously to the heat content, we calculate the transport density of heat instead of the actual heat transport. The transport density of heat is defined as $Q = Q^*/L$ with units W/m, where Q^* is the heat transport and L is the width of the current. This simplification is made because the width of the current is unknown, since measurements only exist in the vertical. Q is given by

$$Q = \rho c_p \int_{z_0}^{z_1} T(z) v(z) dz \tag{2.3}$$

where $v(z)$ is the velocity. From now on, we refer to the areal density of heat as the heat content, and the transport density of heat as the heat transport for simplicity.

2.5.2 Ekman pumping velocity

On the southern hemisphere, stress on the ocean drives an Ekman transport in the surface layers that is directed to the left of the ocean stress. Gradients in Ekman transport will lead to convergence and divergence, that is compensated by Ekman pumping velocity (w_{EK}). Divergence leads to positive (upwards) Ekman pumping velocities, and convergence leads to negative (downwards) velocities. The Ekman pumping velocity is also influenced by the coriolis parameter and water density through

$$w_{EK} = \frac{1}{\rho}\left[\frac{\partial}{\partial x}\left(\frac{\tau^y}{f}\right) - \frac{\partial}{\partial y}\left(\frac{\tau^x}{f}\right)\right] \tag{2.4}$$

where w_{EK} is the Ekman pumping velocity, τ is the wind- and ice-induced stress on the ocean surface, and f is the coriolis parameter.

2.5.3 Ocean surface stress and its dependency on sea ice

Ocean surface stress is not measured directly, but must be modelled or parameterized. In this study, we use four methods to obtain the ocean surface stress (section 3.2.3). The main difference between these methods is how, or if, they include sea ice cover.

The ice acts as an isolating layer, hindering efficient transfer of properties such as momentum and heat between the atmosphere and ocean (e.g. Martin et al., 2016). A thin ice cover is generally more easily affected by the wind stress and thus able to transfer more momentum into the ocean than a thick ice cover (Martin et al., 2016).

The effect of sea ice on momentum transfer is not easily described due to the differences in roughness of the ice. The roughness on top of the ice determines the drag from the wind on the ice, while the roughness on the underside of the ice determines the drag from the ice on the ocean. If the ice is smooth (low roughness), momentum will not be transferred into the ice. Sea ice hinders momentum transfer as long as the roughness of the ice is less than the ocean roughness (Martin et al., 2016). If, however, the roughness of the ice is larger than the ocean roughness, the momentum flux might increase (Martin et al., 2016). The momentum flux typically reaches a maximum at about SIC $= 80 - 90\%$ (Martin et al., 2016). At these concentrations the deformation rates of the ice is high, which leads to high roughness and high momentum flux, while at higher concentrations than 90% the internal stress in the ice leads to a decrease in momentum flux. The sea-ice velocity can be used to infer stress at the ice-ocean interface (Dotto et al., 2018), but surface roughness is still unknown.

We follow the methods presented by Dotto et al. (2018) and Andreas et al. (2010), and relate the results of these methods to the reanalysis results from ERA 5 (ECMWF, 2017). These calculations of ocean surface stress does not consider the nuances concerning the roughness of the ice, or the movement of the ocean under the ice.

Dotto et al. (2018)

Dotto et al. (2018) calculate ocean surface stress τ based on ten meter wind, ice velocity and SIC as follows,

$$\overrightarrow{\tau} = \alpha \overrightarrow{\tau}_{ice-water} + (1-\alpha)\overrightarrow{\tau}_{air-water} \tag{2.5a}$$

$$\overrightarrow{\tau}_{ice-water} = \rho C_{iw} |\overrightarrow{U}_{ice}| \overrightarrow{U}_{ice} \tag{2.5b}$$

$$\overrightarrow{\tau}_{air-water} = \rho_{air} C_d |\overrightarrow{U}_{air}| \overrightarrow{U}_{air} \tag{2.5c}$$

where α is the SIC, $C_{iw} = 5.50 \times 10^{-3}$ is the drag coefficient between ice and water, $\vec{U}_{ice}$ is the velocity of the ice, $\rho_{air} = 1.25\text{kg m}^{-3}$ is the density of air, $C_d = 1.25 \times 10^{-3}$ is the drag coefficient between air and water, and U_{air} is the ten meter wind. $\overrightarrow{\tau}_{ice-water}$ is the stress induced by the ice on the water, while $\overrightarrow{\tau}_{air-water}$ is the wind stress on open water. When calculating τ based on Eq. 2.5a, the stress from ice on the ocean and the stress from the wind onto the ocean is calculated for each grid cell separately. Then the magnitude in each grid cell is weighted based on the SIC in the grid cell and combined to produce the total ocean surface stress. The method does not include the movement of the ocean itself, which means that when SIC is close to 100% and the sea ice is not likely to move much, the calculations result in zero ocean stress. This result is not necessarily correct due to the currents that may flow underneath the ice cover. None of our methods take this into account. The method gave a realistic estimate of ocean surface stress in the studies by Dotto et al. (2018).

Andreas et al. (2010)

Andreas et al. (2010) provide another parameterization for the surface stress on the atmosphere, where the drag coefficient C_d is taken to be a function of SIC. Attempts have been made to include additional variables in the parameterization, for instance the size and ridge height of ice floes (Lüpkes and Birnbaum, 2005), but this makes any computation very demanding, and it is information we do not have. By substituting C_d in Eq. 2.5c with

$$10^3 C_d = 1.500 + 2.233\alpha - 2.333\alpha^2, \tag{2.6}$$

the basis is still the ocean stress induced by the ten meter wind, but SIC is included through the drag coefficient. This parameterization takes into account that the drag increases with increasing ice concentration up to SIC = 48%, after which it starts to decrease again. Note that for this parameterization, we do not further calculate τ, but stop after inserting Eq. 2.6 into $\overrightarrow{\tau}_{air-water}$.

2.6 Data Analysis

To evaluate the relative importance of the properties described in the previous section, we need a set of tools. In this section we go through three aspects of data analysis: i) correlation, ii) frequency spectra, and iii) filtering of time series.

2.6.1 Correlation

As our aim is to study possible drivers of the observed variability at UIB3, we want to investigate whether the observed parameters depend on, or influence each other. We use correlation analysis to quantify the degree to which the time series co-vary. Note however that even though two time series co-vary and have a high correlation, this does not necessarily mean that the variation in one of the parameters is the cause of the variation in the other: they might both be influenced by the variability of a third parameter (Chelton, 1982).

The normalized correlation coefficient between two time series X and Y is expressed as

$$C_{XY} = \sum_{i=1}^{n} \frac{(X_i - \bar{X})(Y_i - \bar{Y})}{n\sigma_X \sigma_Y}, \tag{2.7}$$

where X and Y are the time series we wish to correlate, $\bar{X}$ and $\bar{Y}$ their means, σ_X and σ_Y are their standard deviations, and n is the sample size. C_{XY} is a number between -1 and 1, which denote negative and positive correlation, respectively. In the case of positive correlation, X increases when Y increases, while negative correlation means that when X increases, Y decreases, or vice versa.

There are several issues we need to consider when correlating time series. The correlation may vary with time, there may be a delay (lag) between similar features in the two signals, and we need to be certain that the calculated correlation value can be trusted, i.e that it is not just the result of chance. We first define and explain issues related to the

robustness of correlation, and then explain aspects that are important in relation to specific choices we make in our calculations.

Level of significance and degrees of freedom

As mentioned, the correlation coefficient C_{XY} is a number between -1 and 1, which we from now on simply call C, following Sciremammano (1979). We calculate a threshold correlation value, Cp, that our estimated C must exceed in order to be significant. If $C > Cp$, we trust that C describe an actual co-variation between the two parameters, and denote the correlation as statistically significant. If, on the other hand $C < Cp$, we have to disregard the correlation due to the probability that it is the result of chance, and we denote the correlation as statistically non-significant. The value of Cp is dependent on the *level of significance* we require, and the *degrees of freedom (DOF)*. We will first define the level of significance and its importance, and then DOF.

The chosen level of significance is what describes how trustworthy any correlation value is. Typical levels of significance are 0.9, 0.95 and 0.99. A 0.99 significance level means that you can be 99% certain that the correlation represent an actual relation between the two signals, and that it is not just the result of random chance. Sometimes a lower significance level can be accepted on the basis that even though it opens up for larger uncertainties in your analysis, you still get an indication of what the correlation might be. Although less certain, such an indication might still be useful.

DOF is a measure of the number of statistically independent data points. When correlating two time series, the DOF is related to the *autocorrelation* of these two time series (Sciremammano, 1979). While correlation (Eq. 2.7) compare two time series to each other, the autocorrelation compare one time series to an equal version of itself that is shifted in time. The faster the autocorrelation drops to zero when plotted as a function of the lag between the two equal time series, the higher the DOF. This means that a high degree of independence between each measurement leads to a high number of DOF.

Cp is inversely proportional to the number of DOF's. For calculation purposes this means that the fewer DOF's, the higher the correlation needs to be in order to exceed Cp, and be significant. We calculate correlation coefficients following Sciremammano (1979), which hold for normalized time series. This procedure requires $DOF > 10$ to obtain levels of Cp that are statistically significant. Consequently we need to make sure that the number of DOF always stays above 10 in our analysis.

Time series of correlation

Since correlation may change with time, we divide our time series into equal and overlapping sections ("windows") that we analyse separately. This enables us to identify time periods with high correlation and with low correlation. The appropriate window length is dependant on the time scale of the variability you want to study. The choice of window length is a compromise between i) resolving the variability at the desired temporal scale, ii) having enough DOF's, and iii) resolving a physically sensible lag. Even though a short window length makes it possible to study correlation on short time scales, information about correlation on longer time scales and the appropriate lag might be lost.

Lagged correlation

A couple of aspects should be considered with respect to time lags. First of all, the time lag should not be of comparable length to the window length. This is because the larger the lag, the shorter the overlapping section becomes, and the DOF decrease. We need to ensure that $DOF > 10$. Second, according to the physics of the system, the lag should be restricted to either positive or negative values depending on which parameter is likely to influence the other.

2.6.2 Spectral analysis

To study the variability of our time series, we calculate frequency spectra. When we perform a spectral analysis on a time series we decompose the time series into pure sine waves of various periods and amplitudes using Fourier transforms. Per definition, if the time series was infinitely long, the superposition of the resulting sine waves should recreate the original signal. The frequency decomposition enables us to look into which frequencies influence our time series the most, i.e., have the highest amplitude. The power spectral density (PSD) is the measure of energy at each frequency: if there is a peak at a specific frequency, we know that there is variability at this frequency in our time series.

To reduce uncertainty and obtain a smooth frequency spectra, we divide the time series into overlapping windows, evaluate the spectra of each window and take the mean of these spectra as a representative spectra of the whole time period. The shorter window length we chose, the more windows will fit within the time series, and the smoother our frequency spectra becomes. However, the window length also determines what periods we can resolve. If, for instance, the window length is 80 days long, periods up 40 days can be resolved. This is related to the Nyquist frequency, f_N, which is the highest frequency that can be resolved at a given sample rate, f_s. $f_N = 0.5 f_s$ which means that signals with frequencies higher than f_N will be distorted when sampled with the sampling rate f_s. In spectral analysis,

when the overlap of windows is 50%, $DOF = 1 + n$, where n is the number of windows. We need to make a compromise between what periods we can resolve and how representative our spectra is of the true variability of the time series. The shorter windows we have, the more DOF's, and the more trustworthy it is due to the large basis for averaging, but in turn we get no information about PSD on the long periods.

When looking at similarities between the frequency spectra of two different variables, it may be useful to look for frequencies that have high PSD in both time series. At frequencies where this is the case we say that the time series have high *coherence*. Accordingly, if one of the time series have high variability at a specific frequency, and the other time series have low variability at the same frequency, the coherence is low in this frequency range. As for correlation, we need to check that the coherence is significant. We calculate the number of DOF's (which is dependent on the number of windows), and based on this we evaluate a threshold value for the coherence. This threshold is called the confidence limit, and as long at the calculated coherence exceed this limit, the coherence is significant.

2.6.3 Signal filtering

It is useful to apply different filters to time series, depending on which features we want to study. If we want to focus on seasonality, we might want to remove the distraction of variability on small time scales. On the other hand, if we are only interested in daily variability, the signal of fortnightly tides and seasonality might be the distracting aspects that we want to filter out. To achieve this, we design filters where we assign which frequencies we want to remove from our signal, and which frequencies we want to maintain. It is however not possible to design a filter that admits exactly the frequencies we need, and disregards all others. When we decide the limits of which frequencies we want to study, and which we want to disregard, we have to assign an interval at each frequency boundary where we can force the unwanted frequencies to near zero.

In a lowpass filter, the variability with long periods are maintained, and the short periods are disregarded. A band pass filter maintains variability in a specified range of periods. It can be designed by combining two low pass filters where one admit periods longer than the high frequency boundary of the range, while the other admit periods longer than the low frequency boundary of the range. A time series that is first filtered by the lowpass filter admitting the shortest periods, and then an equal time series that is filtered at the period of the longer boundary is subtracted from the first, the result is the desired band passed time series.

Chapter 3

Methods

To describe the hydrography, heat content and heat transport, ocean surface stress and Ekman pumping in the study region, we have combined several datasets. In this chapter we describe these datasets, and the adaption of theoretical calculations from section 2.5 into methods that can be used for calculations on discrete measurements. We also explain our choices regarding filtering, calculations of correlation, and spectral analysis.

3.1 The moorings

During the ANA06B cruise in 2016, UIB3 was deployed along with three additional moorings from the University of Bergen (UiB), and several other moorings from KOPRI and Gothenburg University. They were recovered two years later in 2018, resulting in mooring data from all troughs leading up to the many fronts of the Getz Ice Shelf. All four moorings from UiB collected both hydrographic and current velocity measurements. Fig. 3.1 shows their location and the observed mean current during these two years, and table 3.1 summarizes the main details of the four UiB moorings.

The moorings UIB1 and UIB4 were placed close to the ice shelf on the east side of the Siple trough, west of Siple Island, to capture the inflow of warm water, while UIB2 was placed further south-west in the outflow region, in the hope of capturing a mixture of meltwater flowing out from beneath the ice shelf.

UIB3 was located in a trough (the "UIB3'trough") on the east side of Siple Island, an area which has been observed to be cooler in summertime than the western side of the island (Jacobs et al., 2013). This mooring-site was chosen to study the possible inflow of warm water towards the Getz Ice Shelf from the other side of Siple Island, and to describe

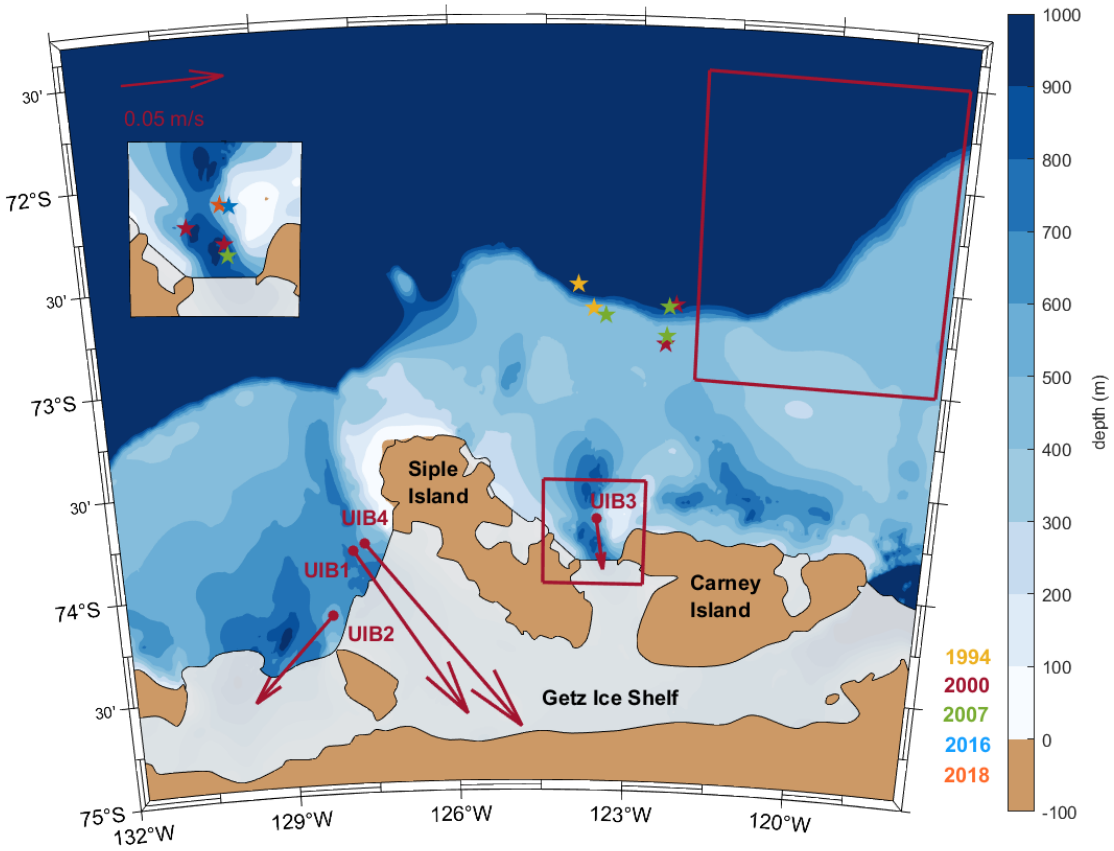

Figure 3.1: The position of all four UIB moorings, and their mean current velocities. The large red box is used for calculation of ocean surface stress, and the stars are CTD stations. The colors indicate which year the stations were taken. The inset in the upper left corner shows the position of the CTD-station taken in the UIB3-trough.

the wintertime conditions. Just like UIB1 and UIB4, UIB3 was located on the eastern side of the trough, about 30 km away from the ice shelf to study the in-flowing water masses. The optimal situation would have been to have measurements from both sides of the trough to quantify the oceanic heat flux towards the ice shelf and its contribution to basal melt. Detailed multibeam data taken from the ship directly before deployment revealed that the bathymetry provided by IBCSO is poor in this area (Fig. 3.2, and Lee, 2016). The apparent ridge in Fig. 3.1 right by UIB3 that seem to separate the trough in one northern and one southern part does not exist, and instead the two parts of the trough is connected by a narrow channel at a depth of about 850 m.

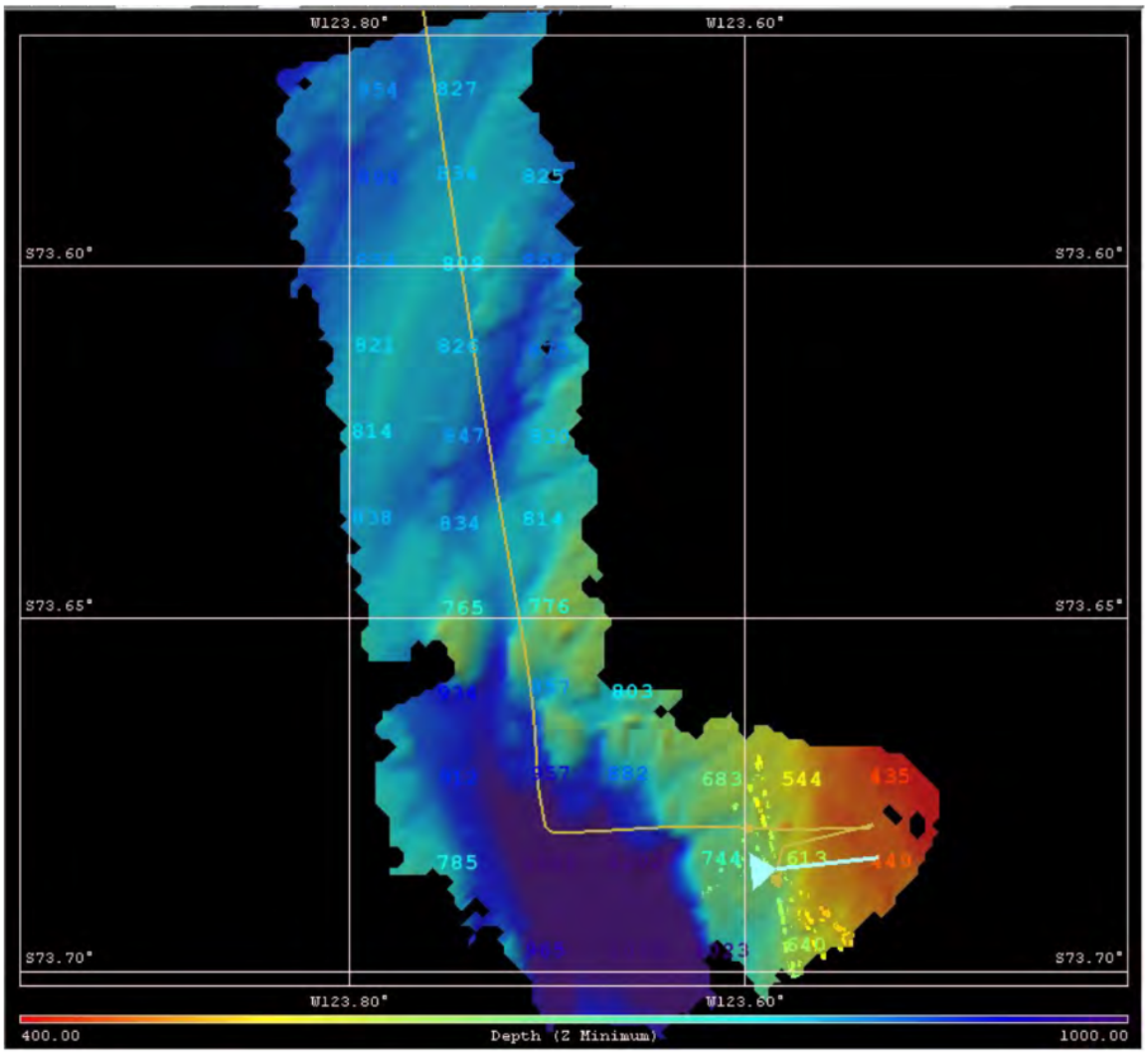

Figure 3.2: Detailed bathymetry at the mooring site in the UIB3-trough obtained with multibeam before deployment of UIB3 (Lee, 2016)

	UIB1	**UIB2**	**UIB3**	**UIB4**
Latitude	-73.8300	-74.1383	-73.6860	-73.7928
Longitude	-127.7930	-128.2153	-123.5841	-127.5996
Deployment	28/01/2016	28/01/2016	30/01/2016	29/01/2016
Recovery	18/01/2018	19/01/2018	31/01/2018	18/01/2018
Depth	707 m	591 m	648 m	609 m
Length	402 m	310 m	352 m	252 m

Table 3.1: Details of the four UIB moorings deployed during the ANA06B cruise.

Three different types of instrumentation were attached to UIB3 (Fig. 3.3):

- SBE37 from Seabird Electronics: conductivity, temperature and depth (CTD) measurements at 27, 252 and 352 m above the bottom. Sampling frequency: 6 times/hour.
- SBE56 from Seabird Electronics: temperature measurements at 52, 102, 152, 202 and 302 m above the bottom. Sampling frequency: 1 time/min.
- RDI ADCP (150 kHz): downward looking acoustic doppler current profiler (ADCP) positioned at 252 m above the bottom, measuring velocity every 8 meters resulting in 29 levels of velocity measurements. Sampling frequency: 1 time/hour.

The data from all moorings were prepared as hourly averaged values, the ADCP data were processed by the RDI software, outliers were removed and finally corrected for magnetic declination to adjust for the offset between the magnetic and geographic southern poles, before collected in a .mat file by K. Assmann. We present salinity as absolute salinity, S_A (g/kg), and temperature as conservative temperature, θ (°C), following TEOS-10 (IOC et al., 2010). Consequently, the pressure difference between the levels of measurements are accounted for. For these hydrographic calculations and calculation of density, we use the 3.0 Gibbs-SeaWater (GSW) Oceanographic Toolbox (McDougall and Barker, 2011).

Rotation of coordinates at UIB3

Fig. 3.1 indicate a mean current direction of south south-east past UIB3. We therefore rotate the coordinate system so that the y-axis is aligned with the mean current averaged over both time and depth, instead of in the north/south direction. This rotation means that the mean u-direction velocity becomes zero, and that a current flowing perfectly in negative y-direction does not flow towards the south, but is shifted with an angle of 9.6°towards the east. Positive u-direction is up-slope, and positive v-direction is along-slope, away from the Getz Ice Shelf, i.e. the mean current is in the negative v-direction.

3.2 Additional datasets

In this section we present the bathymetric data, additional hydrographic data, data needed for calculations of ocean surface stress, sea ice concentration (SIC), and the records of the SAM-index.

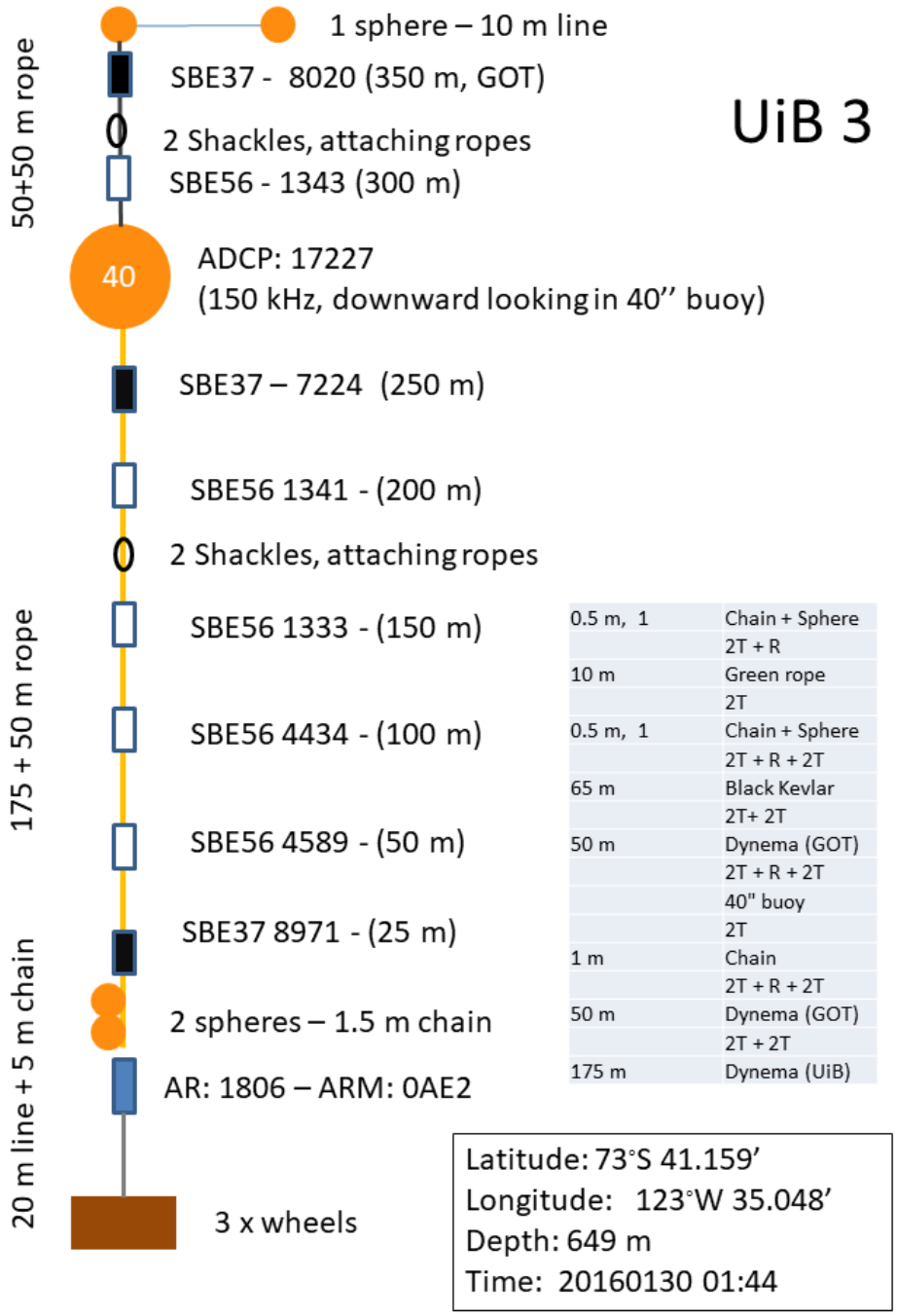

Figure 3.3: The mooring design of UIB3 (Lee, 2016).

3.2.1 Bathymetry from IBCSO

We use the International Bathymetric Chart of the Southern Ocean (IBCSO) Version 1.0 (Arndt et al., 2013) to display bathymetry. This bathymetric model has been available since 2013, and was a great improvement to previous bathymetric representations (Nitsche et al., 2007). It has a resolution of 500×500 meters and includes the sea-floor on all longitudes south of 60°S. To achieve this high resolution, all available bathymetric data consisting of multibeam and single-beam echo soundings, nautical charts, regional bathymetric compilations, and predictions were compiled in the bathymetric model that produce the IBCSO dataset. Despite the high resolution it should be noted that 83% of the grid cells do not contain actual measured values, but are evaluated based on interpolation, or predictions of bathymetry, and that there are large variation in data coverage between different regions (Arndt et al., 2013, their Fig. 1). The Eastern Amundsen Sea near Pine Island Bay and Dotson Ice Shelf (Fig. 2.1) is well covered, while the area further west at the location of the UIB moorings is more sparsely covered.

This means that although we use the IBCSO bathymetry, we need to acknowledge that the uncertainties in our area are large. This is illustrated by the difference between the IBCSO bathymetry and the high resolution bathymetry obtained before deploying UIB3 (Fig. 3.1, and 3.2). Another example that has importance for us is that the ridge that extend north from the eastern end of Carney Island is shallower, and that the apparent channel cutting through the same ridge from east to west is probably less prominent than indicated by IBCSO (personal communication, K. Assmann). The IBCSO bathymetry thus gives us a good general indication, but we must be aware of its uncertainty, especially regarding the details. The location of the shelf break is fortunately relatively certain as it is easy to detect such a rapid change in bathymetry, and the data coverage along the shelf break is high. For all our maps, we use the m_map package developed by R. Pawlowicz (Pawlowicz, 2019).

3.2.2 Hydrographic data

To provide a hydrographic context to our mooring observations, we extract CTD stations from previous cruises with *N.B. Palmer* (1994, 2000 and 2007) and *Araon* (2016 and 2018). The main focus of these cruises were on the areas east and west of UIB3, so none of them provide sections crossing the shelf break towards UIB3. We selected the 12 stations marked with colored stars in Fig. 3.1 to help in the description of the hydrography. The exact dates of the stations are indicated in table 3.2

In addition to these profiles, a seal tagged through the MEOP project (Marine Mammals Exploring the Oceans Pole to Pole, Mcintyre et al., 2017), stayed around the UIB3 mooring site for a few days in March 2014. The seal was tagged with an instrument that

Year	Mooring-site	On-shelf	Off-shelf	Ship	Reference
1994		28. Feb	27.Feb	N.B. Palmer	WOD
2000	1. March	8. March	8. March	N.B. Palmer	WOD
2007	1. March	18. Feb & 10. March	18. Feb	N.B. Palmer	WOD
2014	12-16 March			MEOP	Mcintyre et al. (2017)
2016	29. Jan			Araon	Lee (2016)
2018	21. Jan			Araon	Lee (2016)

Table 3.2: The dates of the CTD-stations used in this study. CTD-data from the N.B. Palmer cruises in 1994, 2000 and 2007 are available through the World Ocean Data Base (WOD).

collects CTD-data each time it returns back to the surface after a dive. The instruments fall off during the molting season, which means that these seals make data collection during winter possible without moorings. We selected 23 profiles in direct proximity to the mooring site as shown by the colored markers in Fig. 3.4: eight as the seal swam westwards north of the UIB3-trough, four following the northern part of the trough, five in the southern UIB3-trough and six as is swam eastwards.

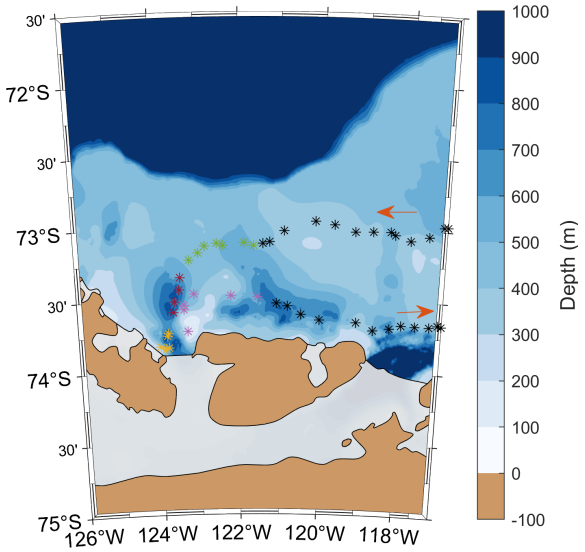

Figure 3.4: The track of "our" CTD-seal. Arrows indicate its swimming direction, and the colors of the markers correspond to the temperature profile in Fig. 4.3. Black markers are dives that are not included in Fig. 4.3

3.2.3 Ocean surface stress and sea ice concentration

We use ocean surface stress estimated in four different ways to study the importance of including properties of sea ice:

τ_{ERA5}**:** The mean turbulent ocean surface stress provided by ERA 5, which is the stress used by Assmann et al. (2019) in the study of the UIB moorings in the Siple trough,

τ_{no-ice}**:** The wind stress on the ocean without any inclusion of sea ice (Eq. 2.5c),

τ_{Cd}**:** Inclusion of SIC as part of the drag coefficient of air on water, Cd, following Andreas et al. (2010), (Eq. 2.6, section 2.5.3), and

τ_{ice}**:** Inclusion of SIC and sea ice movement following Dotto et al. (2018), (Eq. 2.5a, section 2.5.3)

To calculate these ocean stresses, we need information about the ten-meter wind, sea ice concentration, and sea ice motion which we obtain from the sources described below.

ERA 5

The reanalysis product ERA 5 is produced by the European Centre for Medium-Range Weather Forecasts (ECMWF, 2018). Reanalysis use a combination of observations and models to produce an organized data set on both temporal and spatial scales, running back in time. Because it describes the atmosphere and oceans in such an organized way over the past few decades for the entire globe, it is commonly used for assessing climate change (ECMWF, 2018). ERA 5 provides global hourly data with an uncertainty of three hours from 1979 up to today, on a 31 km grid (Hersbach et al., 2019). We use SIC (6h), ten-meter wind (3h), and τ_{ERA5} (3h) from ERA 5.

Ice motion

The National Snow and Ice Data Center (NSIDC) provides data on ice motion. We use the Polar Pathfinder Daily 25 km EASE-Grid Sea Ice Motion Vectors, Version 4.1, which was released in April 2019 (Tschudi et al., 2019). While the other data sets we use are oriented on a grid based on latitudes and longitudes, this data set is gridded with cartesian coordinates. The (x, y) coordinates are projected onto the 25 km Equal-Area Scalable Earth (EASE) Grid. The EASE Grid is used by the NSIDC because it minimized the aerial distortion over the poles, but as all the other data sets we use are gridded based on

latitudes and longitudes, we choose to transfer the ice-motion onto this grid, although the lat-lon projection neither conserve shape, nor area (NSIDC, 2019).

The ice motion vectors therefore have to be transformed from the (x, y) coordinates, to polar coordinates which are positive towards the east and north. Keeping in mind that our area is in the southern hemisphere, the conversion is dependent on the longitude, lon, as follows:

$$u = u\cos(lon) + v\sin(lon) \tag{3.1a}$$

$$v = -u\sin(lon) + v\cos(lon) \tag{3.1b}$$

After converting the ice motion vectors from being oriented in the (x, y) direction to the north/east direction they can be used in calculations of ocean surface stress following the parameterization presented by Dotto et al. (2018). It should be noted that the ice motion is not resolved along the coastline, and that as we get our SIC from ERA 5 and the ice motion from NSIDC, this is a possible source error in our computations of ocean surface stress.

Interpolation

The data sets described above differ in both spatial and temporal resolution. All data from UIB3 are already averaged into hourly values, we have SIC for every sixth hour, ice motion every day, and ten-meter wind and surface stress from ERA 5 every third hour. For calculations of ocean surface stress we linearly interpolate all values to three-hourly data and onto the ERA 5-grid for ten-meter wind. We use the ERA 5-grid because it has higher resolution than the ice-coverage, and the ice-motion data is on a cartesian grid. For calculations including UIB3, e.g. when calculating correlation between ocean surface stress and inflow velocity, we interpolate to hourly values.

3.2.4 Southern Annular Mode

Time series of the SAM-index is provided by the National Oceanic and Atmospheric Administration (NOAA, 2019). We extract data on the index from the deployment period, and define positive (negative) periods as the historical mean $\pm$ 1.5σ, where σ is the standard deviation. This enables us to study the characteristics of the area during anomalously strong positive and negative modes of SAM (Fig. 3.5) in order to see how our area respond to the SAM-variability.

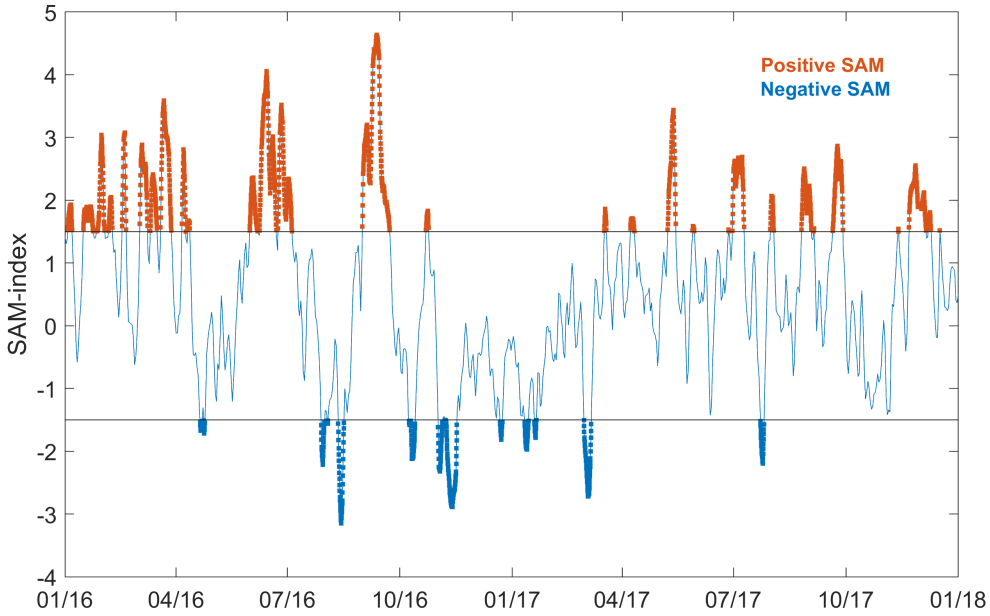

Figure 3.5: Timeseries of the SAM-index for 2016-2018 (Mo, 2000), with defined positive (negative) periods marked with red (blue) dots.

3.3 Discretization of calculations

In section 2.5 we described the theory behind calculations of heat content, heat transport, Ekman pumping velocity and ocean surface stress. The different methods of ocean surface stress were defined in section 3.2.3, and in this section we describe how we adapt the other functions from section 2.5 into discrete expressions that are suitable for our measurements.

3.3.1 Heat content and heat transport

Since UIB3 has eight levels of temperature measurements (Table 3.3), the total heat content has to be calculated as a sum of the heat content in eight layers based on the levels of measurements. This is instead of evaluating the heat content as an integral of temperature as a continuous function of depth (section 2.5.1). Using this approach we calculate the heat content, H, for each time step, where $T(z_i)$ is the temperature at depth z_i, as follows:

Sensor	m.a.b.
CTD	352
T	302
ADCP	252
CTD	252
T	202
T	152
T	102
T	52
CTD	27

Table 3.3: The depth of the sensors on UIB3 in meters above the bottom, m.a.b.. The ADCP measured velocity every 8^{th} from 241 m to the bottom.

$$[z_0, ..., z_8] = [0, 27, ..., 352] \tag{3.2}$$

$$\Delta T_i = T(z_i) - T_f \tag{3.3}$$

$$\Delta z_i = z_i - z_{i-1} \tag{3.4}$$

$$H = \sum_{i=1}^{8} \rho c_p \Delta T(i) \Delta z_i, \tag{3.5}$$

ρ is 1028 kg m^{-3} ans c_p is 3985 J kg^{-1} K^{-1}. z_i is the meters above the bottom, m.a.b., of the instruments of temperature measurements on UIB3. $z_1 = 27$ is the bottom instrument. T_f is the in situ freezing temperature of sea water. We use the temperature relative to the freezing temperature to relate the heat content to the potential for ice melt. The result is a time series showing the variation in total heat content in the lower 352 meters of the water column at UIB3.

To quantify the oceanic heat flux, a closed volume budget is needed. In our region, this means a closed budget encompassing in- and out-flow at every front of the entire Getz Ice Shelf. We only have one mooring supplying data from this ice shelf front, and the bathymetry underneath the ice shelf is highly uncertain, so to circumvent this issue, we again use temperature relative to the freezing temperature.

The mooring measured temperature and velocity at different levels. This means that we need to interpolate, so that the depths of temperatures and velocities match. Velocity was measured at 29 levels between 17 and 241 m.a.b., and temperature at 8 levels between 27 and 352 m.a.b. (Table 3.3). We hence disregard the upper two levels of temperature measurements and interpolate the remaining six levels to the levels of velocity measurements. As most of the heat is found in the deep layers of the water column we accept the resulting

error in the estimation. After interpolating, rotating the coordinate system (section 3.1), and adjusting $T(z_i)$ to $\Delta T(z_i)$, we calculate the heat transport in the along-slope direction at each level, and take the sum of all depths.

$$[z_0, ..., z_{29}] = [0, 17, ..., 241] \tag{3.6}$$

$$\Delta T_i = T(z_i) - T_f \tag{3.7}$$

$$\Delta z_i = z_i - z_{i-1} \tag{3.8}$$

$$Q = \sum_{i=1}^{29} \rho c_p \Delta T(i) v(z_i) \Delta z_i, \tag{3.9}$$

where $v(z_i)$ is the v-velocity at each depth. The result is a time series showing the variation in heat transport per width in the lower 241 meters of the water column at UIB3.

Note that when calculating heat content and heat transport per width relative to the freezing temperature, the result is an estimate of the upper limit. Consequently, estimates of the amount of ice that could be melted by this heat is also an upper limit, where it is assumed that absolutely all the heat available is used to melt ice. Per definition this means that what is calculated is the potential of the incoming water masses to melt ice, and not the actual heat flux. The amount of ice melted therefore has to be less than these estimates. Also, it is not given that all the in-flowing water reaches the ice shelf, it might turn around and flow out of the cavity without coming into contact with the ice shelf. We estimate a average potential for ice melt as follows:

$$M = \frac{\overline{Q} L}{L_f}, \tag{3.10}$$

where M is the mass of ice that melts per second, $\overline{Q}$ is the mean heat transport per unit width during the mooring period, and L is an estimated width of the current. This mass per ice shelf area and the density of ice, gives a rough estimate of the melt rate in meters per year.

3.3.2 Ekman pumping velocity and Ekman pumping

One of the main aims with this study is to investigate whether there is a connection between the Ekman pumping through induced changes in the isotherm height at the shelf break, and the heat content at UIB3. This has been seen to be the case at the moorings west of Siple Island (Assmann et al., 2019).

In section 2.5.2 we described the theory behind Ekman pumping velocity. For simplicity and practical purposes due to the discrete nature of our measurements, we make some adjustments when calculating w_{EK}. Because the average mean winds are in the zonal direction with gradients in the meridional direction, we disregard the dependency of w_{EK} on the gradients in meridional ocean surface stress in the zonal direction, $\frac{\partial \tau^y}{\partial x}$. Following 2.4, this gives us the simplified expression

$$\begin{aligned} w_{EK} \approx -\frac{1}{\rho}\frac{\partial}{\partial y}\left(\frac{\tau^x}{f}\right) &= -\frac{1}{\rho}\left[\overline{\tau^x}\frac{\partial}{\partial y}\left(\frac{1}{f}\right) + \frac{1}{\overline{f}}\frac{\partial \tau^x}{\partial y}\right] \\ - &\approx -\frac{1}{\rho}\left[\overline{\tau^x}\frac{\Delta f^{-1}}{\Delta y} + \frac{1}{\overline{f}}\frac{\Delta \tau^x}{\Delta y}\right]. \end{aligned} \tag{3.11}$$

The coriolis parameter does not change much at high latitudes, so a further simplification disregarding the first term on the right hand side would also be valid. This expression tells us that if the zonal winds increase towards the south, we get convergence in the surface layer due to the gradient in Ekman transport and negative vertical velocities. In the case of divergence, the vertical velocity is positive.

We also look into the Ekman pumping, in order to study the vertical displacement of isotherms due to convergence and divergence in the surface layer. We calculate this based on w_{EK}: first we evaluate the cumulative sum of the vertical displacement from each time step i.e. $w_{EK} \times dt$, where $dt = 3$h is the time between each sampling. We then detrend the signal to get a time series of the cumulative Ekman pumping anomaly in meters.

3.3.3 Practical definitions

The area for evaluation of shelf break processes

We select an area at the shelf break (Fig. 3.1, the "SB-box") to study the possibility that shelf break processes influence the variability in currents and hydrography at UIB3. Several previous studies find that connections between processes in shelf break regions and variability near ice shelves are important (e.g. Assmann et al., 2019; Dotto et al., 2019; Walker et al., 2013; Wåhlin et al., 2013). Inspired by Assmann et al. (2019), and the strong westward ocean surface stress over the shelf break, we chose the position of the SB-box upstream of the UIB3-trough. In hindsight it may have made more sense to choose a shelf break box directly north of UIB3, especially in relation to the possible importance of the along-slope undercurrent, and the locations of the CTD-stations at the shelf break. The wind field is, however, relatively similar in the SB-box and in the shelf break region directly

north of UIB3. The difference between our results, based on the SB-box location, and what they might have been if we had chosen the position of the box slightly further west, is therefore likely small.

The seasons

We divide our two years of mooring data into seasons based on the SIC in the SB-box. When comparing periods of high ice cover, SIC $>$ 80% (winter), to the periods with low ice cover, SIC $<$ 40% (summer), the summers are shorter, and the first summer (S16) is even shorter than the second (S17). In order to make the time series of the summer seasons long enough to meet the conditions for calculating correlation when we apply our bandpass filter, we need to extend the summer season, and relax the criteria of SIC. The time periods we end up with are as follows:

- Summer 2016 (S16): 1. Jan 2016 - 1. April 2016;
- Winter 2016 (W16): 1. April 2016 - 1. Nov 2016;
- Summer 2017 (S17): 1. Jan 2017 - 1. May 2017;
- Winter 2017 (W17): 1. May 2017 - 1. Nov 2017.

This means that when we present our summer and winter seasons, the entire time series is not included, as we try to omit the periods with intermediate SIC.

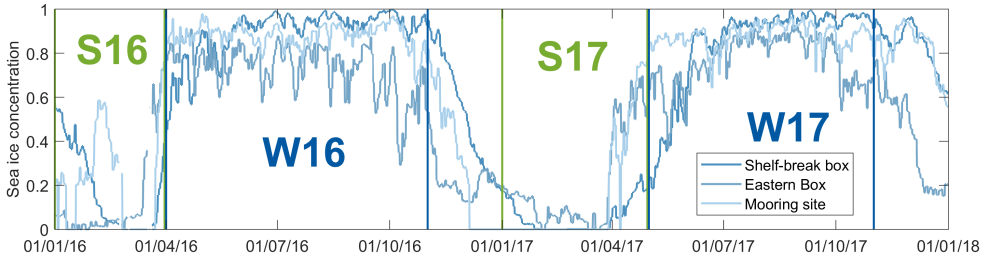

Figure 3.6: The sectioning we use to define the seasons. S16: Summer 2016, W16: Winter 2016, S17: Summer 2017 and W17: Winter 2017.

3.4 Applied data analysis

Several choices and compromises are necessary with respect to filtering of time series, correlation analysis, and computation of frequency spectra. In this section we explain and motivate our choices.

3.4.1 Filtering

We use three different filters. When describing the general evolution over time, we use a lowpass filter that allows periods longer than about two months, When preparing our time series for calculations of correlation we use a bandpass filter that allows periods between about four months to two days in all cases except for one: when investigating co-variation between temperature and salinity at short time-scales at the mooring site, we bandpass filter between 6 hours and 60 days.

When we present time series, the most important aspect is to maintain the general variation in the signal. We therefore apply the two-month lowpass filter in order to avoid unnecessarily chaotic figures, which is the result when including variability on smaller time-scales.

Our bandpass filter allows us to focus our attention on the variability in the range of two days to four months. As we only have two years of data, we can not rely on seasonal signals to be representative for the area: by disregarding variability on longer time scales than four months, we avoid that these periods influence the calculated correlation. Likewise, high frequency signals, such as tides, adds high frequency variability which we do not want to influence our correlation.

In our filter design we use the Butterworth filter which allows us to obtain a maximally flat design. An example of the result of applying the two-day lowpass filter to a time series is shown in the frequency spectra in Fig. 3.7. The green lines are the original Fourier spectra from u- and v-velocities of the current past UIB3, while the black lines are the Fourier spectra from same time series after filtering with the two-day lowpass filter. Note how the lines overlap on all periods longer than two days, and that the PSD is not strictly zero on the periods shorter than two days, but that is decreases rapidly.

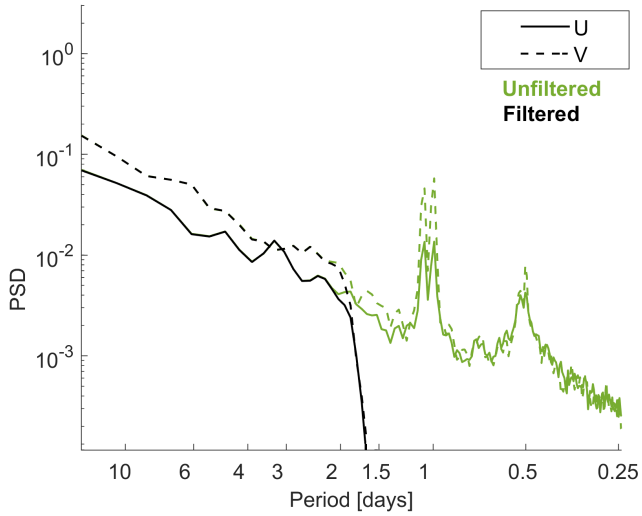

Figure 3.7: An example of the result of using the two day low-pass filter. The green lines are the Fourier spectra from unfiltered velocities past UIB3, while the black lines are the Fourier spectra from filtered velocities.

3.4.2 Moving windows of correlation

To investigate whether the wind stress at the shelf break affects properties at UIB3, such as the heat content, heat transport and the along-slope current at UIB3, we look into the correlation between these variables. We chose moving windows corresponding to 90 days, with an overlap of ten days. As mentioned, with just two years of data, we must be careful when drawing conclusions regarding seasonal signals or trends. This means that choosing a window length of 90 days and thus disregarding the possibility of correlation on a seasonal timescale between the variables does not leave out useful information on the low frequencies. The overlap of ten days enables a relatively continuous evolution of correlation throughout the time series, without demanding too much computation.

We allow a maximum lag of seven days, which is a choice that is not straight forward. The distance from the shelf break to UIB3 is approximately 130 km, and the current velocity past UIB3 is on average 2.25 cm/s in the rotated along-flow direction. This gives an advection timescale of roughly 80 days. 80 days is not a possible lag when using a window length of 90 days, but as we do not expect the velocity past UIB3 to be representative for the entire continental shelf, a shorter lag may be more applicable. We experimented with various lags, and found that a lag of seven days seemed reasonable. Seven days encompass rapid barotropic responses between the shelf break and UIB3, but might however leave out slow advective responses that may bring properties over the continental shelf to UIB3. We allow variability in heat content and along-slope current to lag the ocean surface stress, but

not the other way around, since the properties at UIB3 (at 400-600 meters depth) should not influence the ocean surface stress.

When filtering the signal before correlating, we set the pass band frequencies from two days to four months. The low-frequency limit of four months exceeds the window length of three months, but we still include this lower boundary in order to be sure that the influence of long-term variability is disregarded in our correlation results. The high-frequency limit of two days eliminates the diurnal and semi-diurnal tidal signals to avoid distortion of the correlation by these relatively high frequencies of variability.

We calculate the normalized correlation coefficients, C, and the threshold correlation, Cp, for every window at the 0.95 significance level following Sciremammano (1979). For each window we find the lag with the highest correlation and compare this value to the corresponding Cp value to test for significance. In windows where C is less than Cp, the correlation is disregarded as non-significant. For each time series we present two correlation values: one value for the average of all significant positive correlations, and one value for all significant negative correlations. We also note the number of windows with significant correlation. In the following sections we denote r as the significant correlation, and N as the number of windows with significant correlation. By looking at not only the mean correlation, but also at which time periods that have significant correlation, we get additional information about the characteristics of the time series.

3.4.3 Spectral Analysis

For spectral analysis, we use a Hanning window length of 1024 time steps, which corresponds to about 40 days, and 50% overlap. At this window length, we resolve periods up to about 20 days. 20 days is much less than our upper period limit of four months applied in the band-pass filter, but we chose to disregard the long periods, and in exchange we get a smoother spectra with a higher number of DOF's.

We study frequency and coherence spectra of both the time period as whole, and summer and winter separately (section 4.7). To resolve the same frequencies for these three time periods, we assign the same window length. This results is few DOF's for winter and summer, which is reflected in high confidence limits and less smoothing in their two coherence spectra. The summer season is shortest, and therefore have the highest confidence limit.

Chapter 4

Results

Based on the presented background theory and methods, we now describe our results. As the mooring UIB3 provides new data in our area, and is the center of our study, we start off by describing the observations from the mooring, and the hydrography from selected CTD stations. We then go through the following aspects in respective order:

- The wind field during the two mooring-years
- Variability in the heat content and heat transport observed at UIB3
- Comparison of ocean surface stress estimated with our four methods and the seasonal variability in ocean surface stress and Ekman pumping velocity
- Correlation between ocean surface stress and the along-slope velocity observed at UIB3
- Spectral analysis of ocean surface stress and along-slope velocity
- Variability in the large scale Ekman pumping velocities following the modes of the SAM.

4.1 Mooring observations

The records from UIB3 show how temperature, salinity and velocity varies over time and depth from 2016 to 2018 (Fig. 4.1). Cool and fresh water is overlying warmer and saltier water (Fig. 4.1a,b). This warm water along the bottom is not pure Circumpolar Deep Water (CDW), but lies on the mixing line between CDW and winter water (WW), (Fig. 4.2), and is identified as modified CDW (mCDW). The maximum temperature at UIB3 during the observation period is 0.13°C.

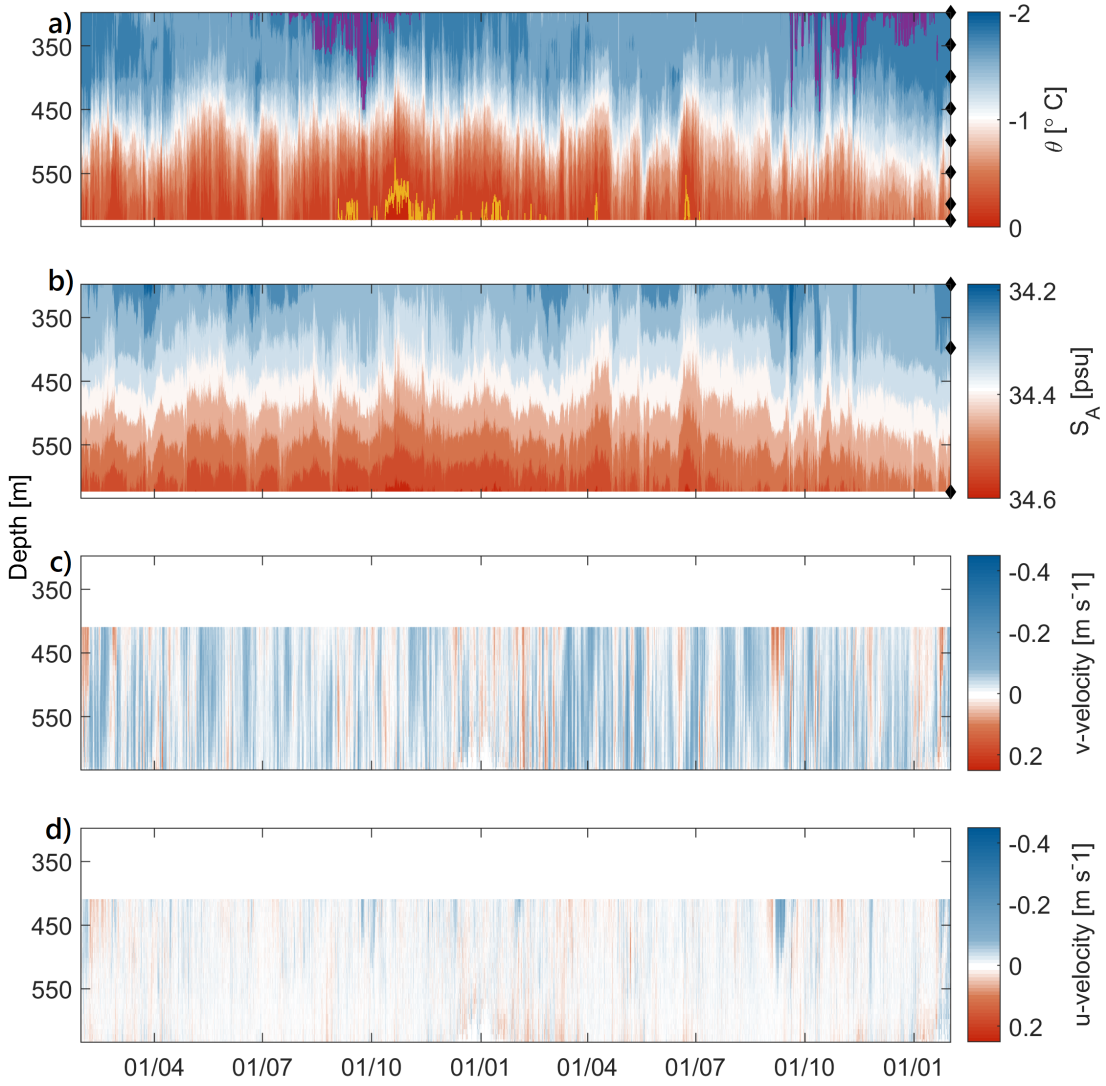

Figure 4.1: Hourly time series from UIB3 showing a) conservative temperature, b) absolute salinity, c) rotated along-slope velocity and d) across-slope velocity. The -1.8° contour is indicated in purple, and the 0° contour in yellow. Depths of instruments measuring temperature and salinity are indicated by the black markers. Velocity measurements were taken at 29 levels (not marked here).

There is no clear seasonal cycle in the time series of temperature and salinity (Fig. 4.1). A period with a thick layer of relatively high temperatures (around 0°C at the bottom) is found from November 2016 to January 2017, while during the same months in 2017 the temperatures are about half a degree lower. There is some evidence of a similar pattern in the salinity data (Fig. 4.1b), with higher salinity from November 2016 to January 2017 than by the end of 2017. On smaller time scales, the general variation in temperature and

salinity is very similar to each other. The average correlation between temperature and salinity is $r = 0.76$ at significance level 0.95, and significant during the whole period when bandpass filtered for 6 hours and 60 days. Both temperature and salinity show variability at tidal frequencies, especially for diurnal periods.

A deepening of the thermocline during winter can be seen in the temperature contours at the end of the winter seasons. The $-1.8°$C isotherm extends down to about 450 meters depth in October 2016 and October/November 2017 (Fig. 4.1). These cold water masses are indications of deep ventilation of surface waters. Note that relatively cold water extends down to 450 meters depth in March 2016 but not in March 2017.

The TS-diagram shows that the observations do not align with the Gade-line (section 2.2), apart from possibly a few occasions at the bottom instrument (620 m depth). This suggests that the water at UIB3 has not been modified by glacial melt in 2016 and 2017, since water masses modified by glacial melt should align with the Gade-line in a TS-diagram (section 2.2).

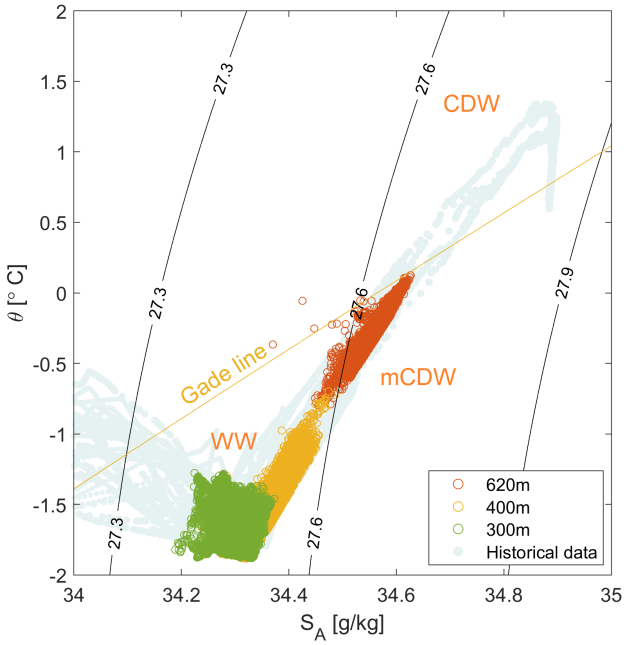

Figure 4.2: TS-diagram for UIB3 with the CTD-seal dives (Fig. 3.4), and selected CTD-stations (Fig. 3.1) in the background. Sigma density contours (black), the Gade-line (yellow), and characteristic water masses are label (WW - winter water, mCDW - modified circumpolar deep water, and CDW - circumpolar deep water).

The two lower panels in Fig. 4.1 show that the rotated velocity (section 3.1) is generally in the negative v-direction, i.e., towards the ice shelf. Fig. 4.1c also shows that the along-

slope current is in relatively constant with depth. There are gradients in strength with depth, but for the most part is has the same direction throughout the water column. The ADCP instrument was located at a depth of 400 m and looking down, so the behaviour of the current in the upper section of the water column is unknown. The velocity in the u-direction (Fig. 4.1d) is particularly weak as a consequence of the rotation of the coordinate system.

From November 2016 and throughout the mooring period, there is significant correlation of $r = -0.42$, $N = 26$ window lengths, between the along-slope current and temperatures below 400 meters depth. The negative correlation indicates that an increase in northward current velocity corresponds to a decrease in temperature. In the beginning of the mooring period there is a short period of positive correlation ($r = 0.36$, $N = 6$). The 2-day to 4-month bandpass filter is applied before calculating this correlation to omit the influence of tides. Variability in both velocities and hydrography is strongly influenced by diurnal tides.

4.2 Additional hydrographic data

In the TS-diagram (Fig. 4.2), and the temperature profiles (Fig. 4.3), we include all CTD-stations marked on the map in Fig. 3.1, as well as the data collected by the CTD-seal. The exact dates the stations were taken are noted in table 3.2, for reference in relation to fraction of melt water in the surface layers, depth of the surface mixed layer and the possibility of recently ventilated WW. We first list the main aspects from the combined data from our mooring and the selected CTD-stations, and then describe the profiles in detail.

- Unmodified CDW is present off the shelf break just north of UIB3 in all off-shelf profiles (1994, 2000, 2007).
- 2000 was cold at depths larger than the thermocline below WW, and there is little difference between the eastern and western side of the trough throughout the profiles.
- 1994 and 2007 were relatively warm.
- The maximum temperature at the mooring site is found in 2014.
- 2016 was close to the temperature maximum in 2007 in the UIB3-trough
- The thermocline below WW is deep in 2018, and the surface mixed layer as well, though not as deep as in 2014.
- The most notable variability in the mooring record is the diurnal signal. There is no indication of seasonality during these years, though there is evidence of deep mixing in winter.

- There is a negative correlation of $r = -0.42$, $N = 26$ between along-slope inflow velocity and temperature, from about November 2016 until the end of the mooring period. Tides are filtered out in this correlation.
- The temperatures were higher during the first part of the mooring record than the last.
- The velocity observed at UIB3 is mostly barotropic, and towards the ice shelf.

A few characteristics stand out in the profiles (Fig. 4.3).
Off-shelf: The observations from the years 1994 and 2007 are very similar: their thermoclines align, and their maximum temperatures are similar, though 2007 is warmest with a maximum temperature of 1.34°C. The off-shelf thermocline in 2000 is deepest.
On-shelf: The western stations from 1994 and 2007 are warmer than the eastern stations from 2000 and 2007. In agreement with the off-shelf profiles, the thermocline was also deepest on-shelf in 2000.
UIB3-trough: The variation in bottom depth between the profiles make them less comparable, but we still see that just as at the shelf break, 2007 was warm and 2000 was cold at the mooring-site. The difference between the years is about 0.5°C. Two profiles were taken at the mooring site in 2000, one at the eastern side and one at the western side of the trough. These profiles are similar in both temperature and salinity. The stations taken at the exact mooring position in 2016 and 2018 do not extend as deep as the other profiles. Still, the thermocline slope and depth in 2016 lies between 2000 and 2007, while in 2018 the layer of WW above the thermocline is much deeper than any of the preceding years, nearly extending down to a depth of 600 meters. Regarding the gradients of the thermoclines, 2018 also stands out with a sharp gradient that is similar to the on-shelf thermoclines, whereas the thermoclines in the other profiles from the UIB3-trough have much weaker gradients.

The profiles from 2018, on-shelf 2007 and on-shelf 2000 all show evidence of freshly ventilated WW between about 200 and 400 meters depth. The profile in 2018 was taken in January, the profile from 2007 in February and the profile from 2000 in March. The profiles with weaker thermocline gradients do not reach these low temperatures.

The maximum temperature at UIB3 is found at the bottom, at 620 meters depth. At the continental shelf break where the sill depth is approximately 460 meters, this same temperature is found in shallower waters, and at about 30 meters shallower depths off-shelf than on-shelf in all cases. These differences are evident from the temperature profiles. Common to all profiles at the shelf break is that the maximum temperature at UIB3 is found in the thermocline below the winter water.

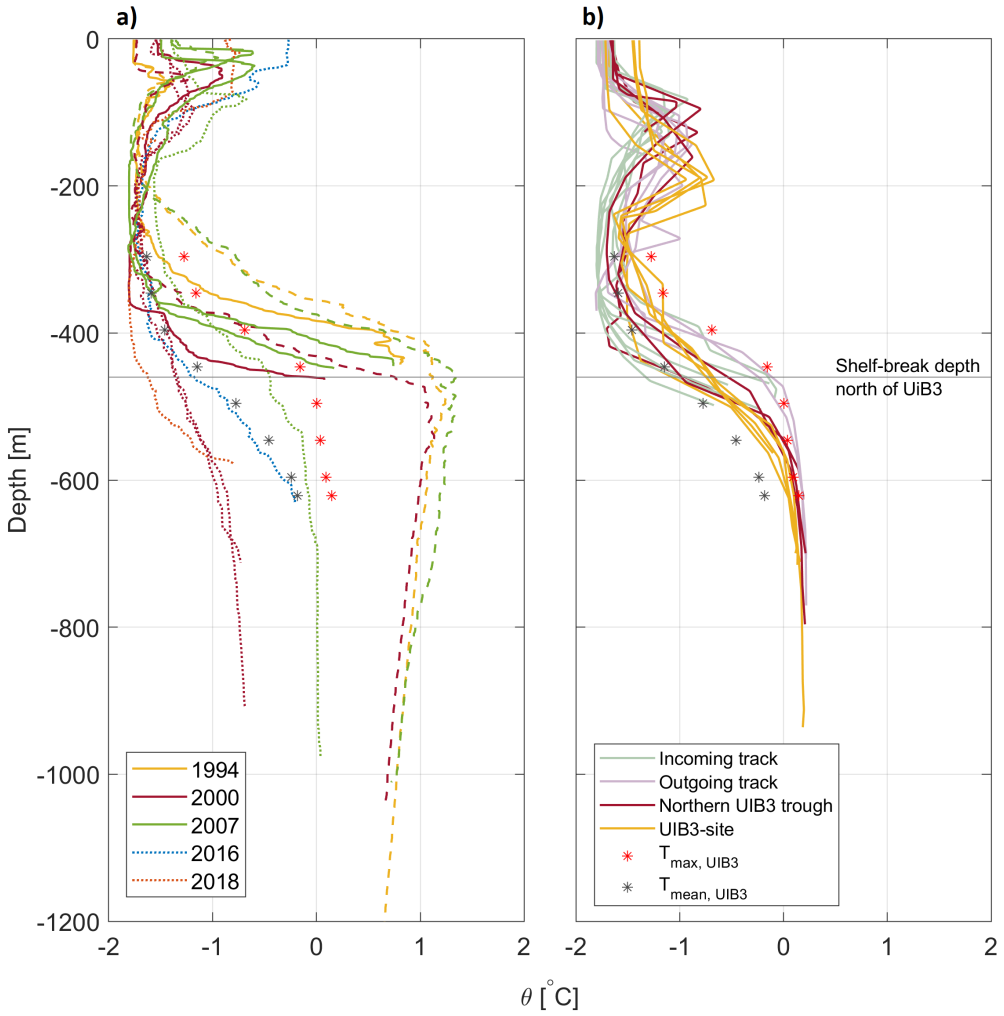

Figure 4.3: Conservative temperature profiles from a) selected CTD-stations, and b) the seal (2014). In a), the coarsely dashed lines are the off-shelf stations, solid lines are on-shelf stations and the finely dashed lines are taken at the mooring-site. The shelf break depth north of UIB3 of approximately 460 meters depth is indicated. The maximum and mean temperatures recorded by UIB3 is indicated by red and grey stars.

Although we are mainly concerned with the deep layers of the profiles, we briefly note a few features in the surface layers.

- In the UIB3-trough:
  - In 2016, the upper 40m are about half a degree warmer than in 2018, and more than one degree warmer than the surface layers in all other years.
  - In 2018 the mixed layer is about 80m deep, which is more than about twice the

depth of the other profiles.

- On-shelf and off-shelf
  - In 2007 the western station is warmer than the eastern at the surface as well as at depth, and the mixed layer is shallower (depth of 20m vs 40m).
  - The layer of WW is thinner in 1994 and 2007, than in 2000. At around 450-500m depth all these profiles have their maximum temperature. 2000 has the lower temperature throughout the profile.
  - The eastern stations (2000 and 2007) have the same mixed layer depth.
  - The stations to the west have smoother profiles than those to the east.

Regarding salinity (not shown), the main difference in the surface layers is between the years, not the location. In 1994 and 2007, the surface is fresher than in 2000, 2016 and 2018. While 2016 and 2018 distinguished themselves from each other and from the other years regarding surface temperature, they both align quite well with 2000 in the salinity profile. The profiles of salinity and temperature on-shelf match nicely, and – in agreement with the results from UIB3 – we see that higher temperatures corresponds to high salinity. Below the pycnocline separating WW from CDW, the salinity is constant and equal for all years off-shelf, and at the mooring-site, the water at depth is fresher than at the shelf break.

The results above are all ship-based CTD-profiles, but as described in section 3.2.2, seals can also provide CTD measurements. One such seal ventured to the UIB3 site in the middle of March 2014. All profiles in Fig. 4.3b are dives taken by this one seal. Compared to the years described above, the bottom temperature at the mooring-site in 2014 was higher, 0.19°C compared with the maximum of 0.04°C in 2007 and -0.7°C in 2000. This is also more than the maximum temperature during the entire two years of mooring data. In general, the mixed layer was deeper in 2014, but the thermocline below the winter water was similar to the other years, i.e., the layer of WW was thin. The mixed layer was deeper in the southern part of the UIB3-trough, than the northern part.

4.3 Seasonal wind field

The wind field from ERA 5 averaged over the defined seasonal periods (section 3.3.3) is shown in Fig. 4.4, together with the winter leading up to the mooring period, and all the zero-contours. The variation is large during our two years of mooring data (Fig. 4.4), and the deviation from the expected seasonality (section 2.1) is notable. Compared to the long-term mean (Assmann et al., 2013), the mean zero-contour is located further south than usual, at about 71.5°S (Fig. 2.2), compared to between 70°S and 71°S.

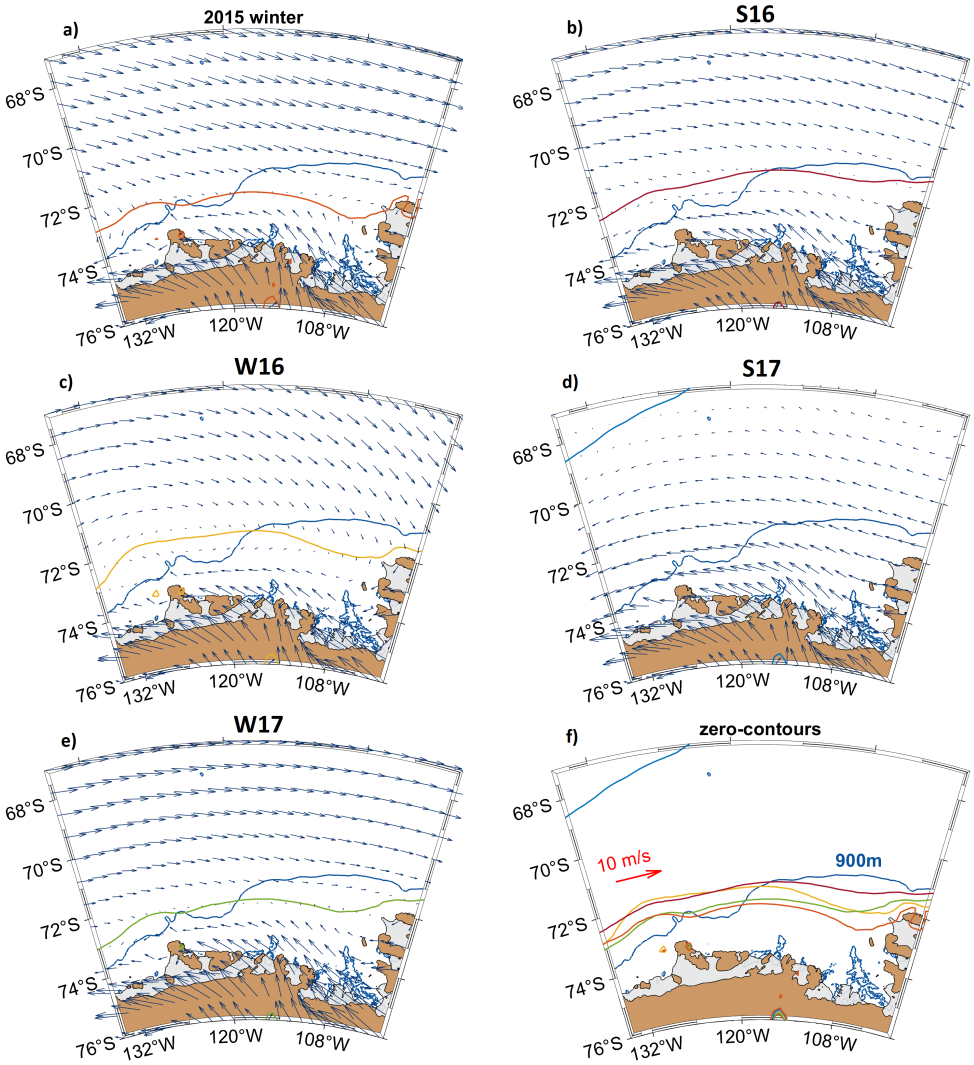

Figure 4.4: The average wind field from ERA 5 during the time periods as defined in section 3.3.3. a) the winter of 2015 preceding the mooring period, b) S16, c) W16, d) S17, e) W17, and f) all zero-contours. The dark blue line represents the 900 meter isobath, and the colored lines indicate the zero-contours for the respective seasons. The scale indicated by the red arrow in the lower right panel is valid for all panels.

The most striking feature in these panels is the large difference between the two summers. The location of the zero-contour during the first summer (S16) is what we would expect during winter (Assmann et al., 2013), while during S17, the zero-contour has shifted into latitudes that are even further north than the average. The three winters are on the other hand similar to each other. During the winter leading up to our mooring-period in

2015, the zero-contour has shifted the furthest south. This winter has the strongest westerlies of the five seasons in Fig 4.4. W16 has the northernmost zero-contour and weakest westerlies of the winter seasons. When studying correlation and coherence in the following sections, we still study S16 and S17 combined, and W16 and W17 combined in order to satisfy criteria needed for the analysis, such as the number of DOF's.

A second feature to note is the circulation pattern. This is especially prominent during W16, where there is evidence of cyclonic circulation with its center north of Siple Island. During W17 there is no evidence of this circulation, and during the winter of 2015 the center is further west. The wind field preceding the CTD-profiles in 2014, 2016, and 2018 were as follows: In January 2016 the circulation center was west of Siple Island with strong southwards meridional winds crossing the shelf from about 123°W and eastwards, while in January 2018 the center was at about 108°W, with strong winds towards the north-west over the shelf break north of UIB3. In March 2014 – right before the CTD-seal profiles – the circulation was less apparent, but had a weak center east of 100°W. The band of westerlies from 70°S and northwards were strong, while the winds over the shelf break were weaker than in January 2018 .

Regarding the wind field over the SB-box specifically (Fig. 3.1), the largest difference is between the winter of 2015 and S17. The winter of 2015 is characterized by strong westerlies over the box, while during S17 easterlies cover the entire shelf break. At the mooring site the winds are constantly relatively strong in a westerly direction. The tendency of a polynya to form at the mooring site is likely connected to these persistent winds (K. Assmann, personal communication).

4.4 Heat content and heat transport

The heat content relative to in situ freezing point at UIB3, averaged over the entire mooring period is $(16 \pm 2) \times 10^8$J m^{-2}, and ranges from 24×10^8J m^{-2} (October 2016) to 9.5×10^8J m^{-2} (January 2018) (Fig. 4.5b). As the heat content is dependent on the temperature and the thickness of the warm layer (section 3.3.1), the general variability in both these variables are reflected in the heat content, with a peak by the end of 2016, and a decrease during the last months of the mooring period. There is no indication of a seasonal cycle during the two years, but a large difference between the two winter periods.

The heat content at the mooring UIB4, located west of Siple Island (Fig. 3.1), is higher and more variable ($17\pm 4\times10^8$J m^{-2}), (Fig. 4.5a), although deployed at a shallower isobath (609m vs 648m). While the heat content at UIB4 follows the Ekman pumping at the shelf break (Fig. 4.5a, 4.6, and Assmann et al., 2019), the heat content at UIB3 does not display any similarity with the Ekman pumping.

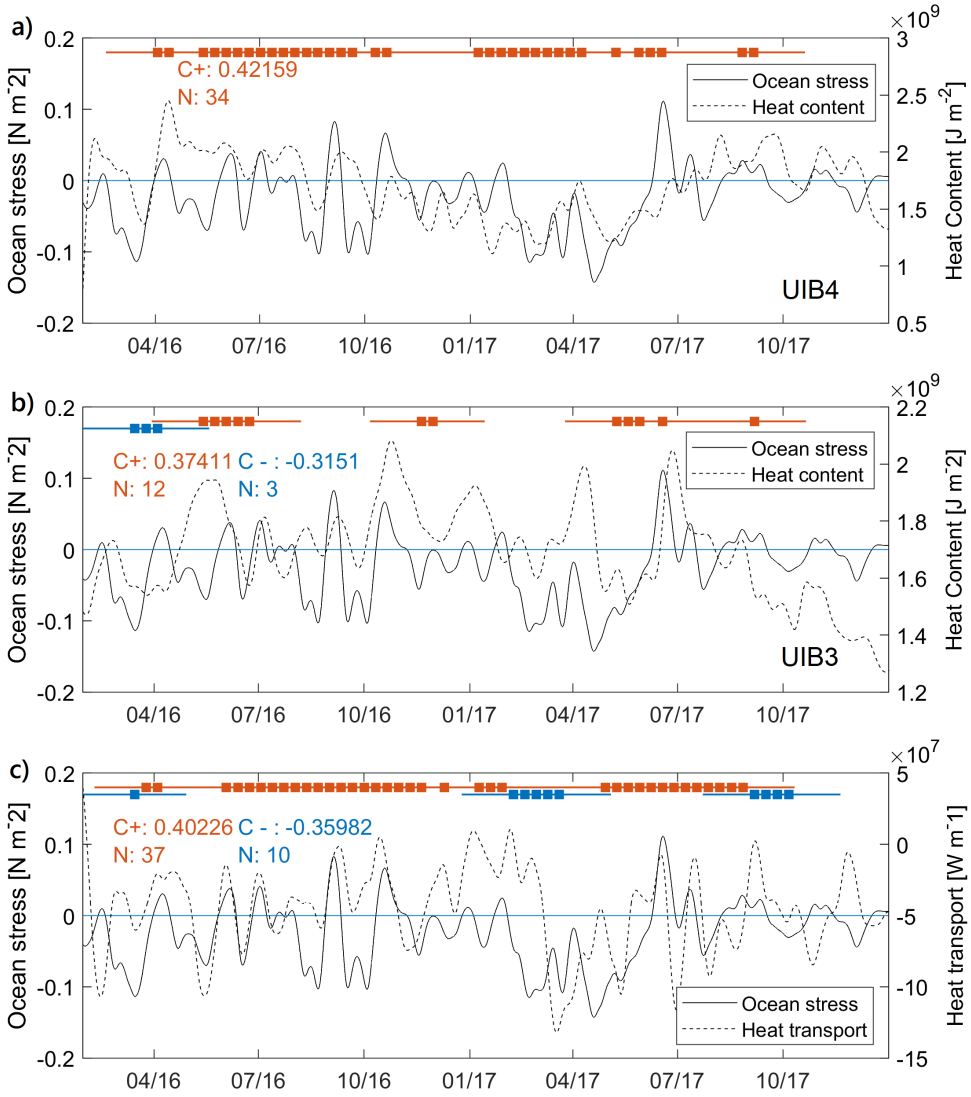

Figure 4.5: Lowpass filtered (2-months) ocean surface stress following Dotto et al. (2018), τ_{ice}, over the SB-box, and heat content at a) UIB4, b) UIB3, and c) heat transport past UIB3. Periods of significant correlation of the corresponding band-pass filtered (2 days to 4 months) time series are indicated by red (positive correlation) and blue (negative) bars. Colored boxes are the center of each 90-day correlation-window.

The internal variability in the time series of Ekman pumping is too low compared to the length of the time series to achieve $DOF > 10$. Since $DOF > 10$ is required for Sciremammano's method to work, this means that we cannot calculate the time series of correlation between the heat content and the Ekman pumping. Instead, we correlate heat content and the ocean surface stress which is an important driver of the Ekman pumping. We use the ocean surface stress following Dotto et al. (2018) from the SB-box for correlation

with heat content at both UIB3 and UIB4 because of the high correlation in ocean surface stress between the two shelf break areas ($r = 0.8$, $N = 65$: all windows). As expected based on the difference in co-variation with Ekman pumping between the two areas, UIB4 has a higher and more continuous correlation with ocean surface stress than UIB3 ($r = 0.42$, $N = 34$ vs $r = 0.37$, $N = 12$, Fig. 4.5).

The heat transport past UIB3 (Fig. 4.5c) follows the variability in velocity, rather than temperature in the way that the heat content does. It ranges from -33×10^7W m^{-1} (May 2017) to 19×10^7W m^{-1} (February 2017), but is on average $(-4.4 \pm 6.3) \times 10^7$W m^{-1}. This means that the general direction of heat transport is southwards past UIB3, towards the ice shelf. Following Eq. 3.10, we obtain an estimate of the ice melt that may potentially be caused by the heat transport in the UIB3-trough. Relative to the entire Getz Ice Shelf, the rough estimate is a rate of 0.6 m/year for a typical current width of 5 km. It is important to note that this is an upper limit, where we assume that all the water is cooled down to the freezing point, and that absolutely all of the heat transported past UIB3 is used to melt ice. In relation to this we also note that we do not have observations of the water flowing away from the ice shelf, and therefore do not know if we would see water that was cooled to the freezing point in such a current.

Whereas the correlation between heat content at UIB3 and ocean surface stress at the shelf break is sporadic, the heat transport has significant correlation throughout most of the period that alternates between positive and negative values ($r = 0.4$, $N = 37$ and $r = -0.36$, $N = 10$, Fig. 4.5c). The positive correlation dominates, which means that increased westwards (eastwards) ocean surface stress at the shelf break corresponds to increased southward (northward) heat transport past UIB3. As the heat transport is mostly dependent on the inflow velocity past UIB3, and exhibits significant correlation with the ocean surface stress at the shelf break, we look into the correlation between the ocean stress and the inflow velocity in detail. We focus our further analysis on this correlation.

4.5 Ocean surface stress and Ekman pumping

As described in section 3.2.3 we calculate the ocean surface stress in three different ways, in addition to using the stresses from ERA 5. The presence of sea ice will affect ocean surface stress, and thus the correlation between the stress and observations from UIB3. Fig. 4.6a compares the time series of the different methods averaged over the SB-box. For the most part the magnitudes are between -0.2 and 0.2 N/m^2, with a tendency to stay in the negatives during summer, and vary about the mean during winter. When studying this figure, recall that τ_{ice}, the ocean stress following Eq. 2.5a from Dotto et al. (2018), is the method we use for further discussion.

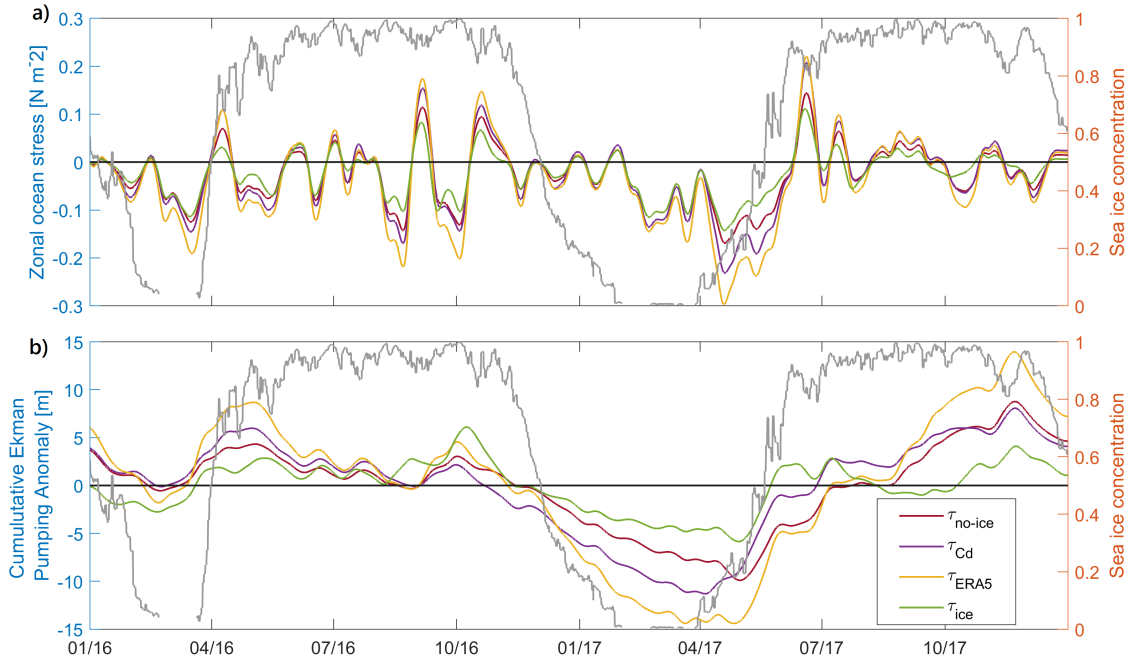

Figure 4.6: Lowpass filtered (2-month) a) zonal ocean surface stress and b) resulting cumulative Ekman pumping anomaly over the SB-box using the four different methods for calculation of ocean surface stress (section 3.2.3). Sea ice concentration is shown in gray

The general pattern that holds for nearly the entire time series is worth noting (Fig. 4.6a). Intuitively we expected that τ_{no-ice}, the most simplified version with no reliance on sea ice, and τ_{ice}, would be the least similar due to the total lack of sea ice dependence in τ_{no-ice}, and the direct inclusion of sea ice in τ_{ice}. This is however not the case. The ocean surface stress generally increases in amplitude from τ_{ice}, followed by τ_{no-ice}, then τ_{Cd}, and finally τ_{ERA5} has the largest magnitude. As expected, the difference between the methods is largest during winter, when the sea ice concentration (SIC) is highest, and τ_{ERA5} often have twice the magnitude as τ_{ice}. Apart from the difference in magnitude, the time series co-vary. The only notable exception from the co-variation are the results of τ_{ice} during the winter 2017. Due to this general co-variation it is reasonable to assume that these different methods of calculating the ocean surface stress should not result in large differences in correlation with parameters at UIB3. Note however that the time series shown here are lowpass-filtered at two months for better visibility, while the time series used for correlation are bandpass-filtered at two days to four months.

The cumulative Ekman pumping anomalies (Fig. 4.6b, Eq. 2.4) generally have the same ranking in magnitude as the zonal wind stress. However, as the Ekman pumping is based on the gradient in the wind stress, not simply the magnitude of the wind stress itself, there are some exceptions, and τ_{ice} causes the strongest Ekman pumping in some periods.

The Ekman pumping during these two years is generally positive in periods of high SIC and negative in periods of low SIC. During summer 2017, from about January 2017 to April 2017, the Ekman pumping is strictly negative, while in 2016 summer, it stays closer to zero. The weak Ekman pumping during S16 coincides with a short period of low SIC (Fig. 4.12) and the absence of summer-time easterlies (Fig. 4.4). The maximum anomaly is induced by τ_{ERA} in 2017: in May the negative anomaly is -15 m, while in December the positive anomaly is 15 m.

4.5.1 Seasonal variability in ocean surface stress and Ekman pumping velocity

Ekman pumping plays an important role in relation to heat content on the continental shelf in several regions of the Amundsen Sea (e.g. Spence et al., 2014; Dotto et al., 2019; Assmann et al., 2019). We therefore look into the spatial distribution of ocean surface stress and the resulting Ekman pumping velocity during our defined summer- and winter seasons. The difference between the time periods might contribute to explaining the variability in the time series of properties such as heat content at UIB3. The atmospheric conditions during the two winters are similar to each other, while S16 and S17 are not (Fig. 4.4), so we study the winters combined, and S16 and S17 separately in this section (Fig. 4.7).

The strongest eastwards ocean surface stress is found in winter (0.11 N m^{-2}), during which the westwards stress over the continental shelf is weak (Fig. 4.7, upper panels). The strongest westwards stress is found during S16 (-0.11 N m^{-2}), although the zero-contour in stress is much further north during S17, which means that the westward stress impact a larger area during S17. The entire continental shelf is however influenced by westward ocean surface stress during both summers. Note the variation in direction and gradients over the SB-box during the different time periods. In winter the northern part of the box is influenced by ocean surface stress from the west, while during both summers the ocean surface stress is from the east over the entire box. In the eastern-box – which will be introduced in the following section 4.6 – the ocean stress is always westwards, though stronger during summer.

The Ekman pumping velocity is generally positive during all seasons (Fig. 4.7, lower panels). Note that the high values along the coast are likely artifacts of the calculation method as we do not take the coastline into account when calculating Ekman pumping velocities. Consequently, we ignore the areas with sudden changes in magnitudes when studying Ekman pumping velocities further, and exclude these values in the magnitudes presented below.

Both winters have upwelling in the area of strong divergence near the zero-contour. W16 has a thin band of downwelling furthest north around 68°S (not shown), indicating that the gradient in ocean stress changes direction. The maximum positive velocities are slightly

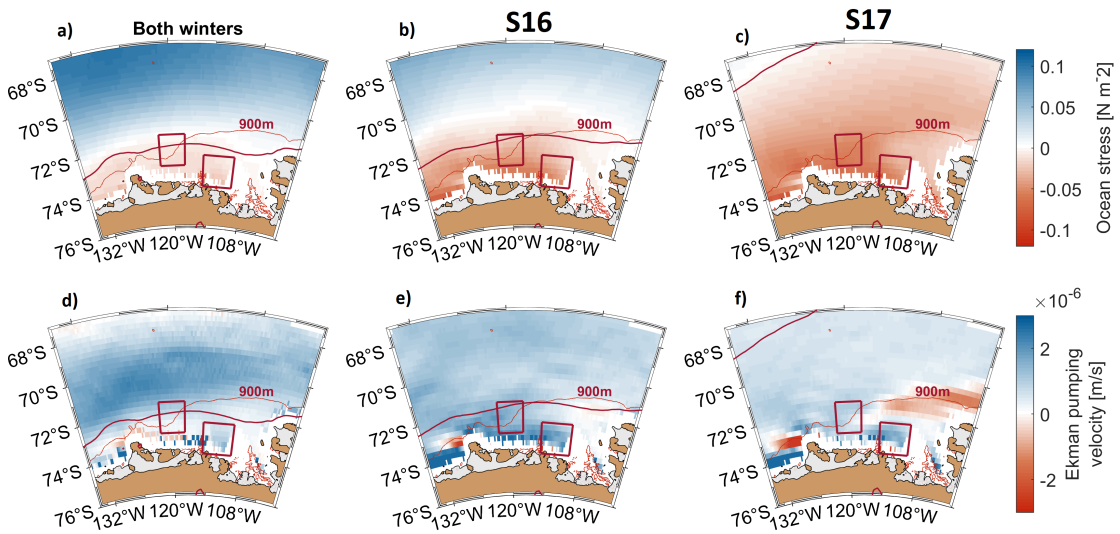

Figure 4.7: Mean ocean surface stress and Ekman pumping velocity over a, d) winter 2016 and 2017, b, e) S16 and c, f) S17. The SB-box, eastern-box, the zero-contours from the wind fields (purple line) and the 900 meter isobath (red line) are included.

higher during W17 than W16 (0.26 m/day vs 0.22 m/day), and W17 also distinguishes itself through the low occurrence of negative velocities over the entire area (not shown). During summer, the positive velocities are more homogeneous than in winter, and generally the velocities are higher during S16 than S17. S17 is characterized by an area along the shelf to the east of our study area with strong negative velocities. The highest positive values along the shelf break and in the two boxes are found during S16.

To summarize, the ocean surface stress during the two summers has large differences. S16 is more similar to the average winter situation than the average summer situation. The strongest westward ocean surface stress is found during S16. During S17, our entire study area is influenced by westward ocean surface stress. Our winters resemble each other, though the strongest eastward ocean surface stress is found the second winter. The mean Ekman pumping velocity is positive and homogeneous both summer seasons, while during winter there is a band of high positive vertical velocities just north of the shelf break.

4.6 Ocean surface stress and the along-slope velocity past UIB3

First, we present the time series of correlation between the along-slope velocity at UIB3 and the four ocean surface stress estimates over the SB-box (4.8). As estimates of correlation are filtered with the 2-days to 4-months bandpass filter, and the time series in our figures are 2-month lowpass filtered, we include Fig. 4.9, which gives an impression of the actual variability in the bandpass filtered, correlated time series. We then study the correlation over the entire Amundsen Sea region to investigate whether ocean surface stress outside our SB-box might affect inflow velocities past UIB3. Finally we select a box at the area where we find the highest correlation, and compare the time series of correlation in this box to the original SB-box.

The estimates of correlation between the along-slope velocity at UIB3 and the four ocean surface stress estimates are in the range $r = 0.39$ to $r = 0.41$, and $r = -0.34$ to $r = -0.38$ for periods of positive and negative correlation, respectively (Fig. 4.8). Both the highest positive and negative correlations are form τ_{ice}. All methods have significant correlation for approximately the same number of windows (N for positive correlation: between 35 and 37, N for negative correlation: between 11 and 14), which makes it meaningful to compare the correlation values. For all methods, the correlation shifts between continuous periods of positive and negative correlation, and just like the variation in Ekman pumping, the pattern seem to co-vary with SIC (Fig. 4.12): periods with high (low) SIC tend to have positive (negative) correlation. The correspondence is strongest during 2016 and the start of 2017. Note that the correlation also follow this pattern for τ_{no-ice} where sea ice is not included.

We now consider the entire Amundsen Sea region. As the correlation varies in time, and shifts between positive and negative correlation at somewhat periodic intervals (Fig. 4.8), we divide the two years into sections when studying the spatial distribution of correlation as well. With only two years of mooring data we cannot assume that this periodic alternation between positive and negative correlation is persistent. Still, it is interesting to look into, as the changes in correlation appears to coincide with changes in SIC. We therefore extract periods based on three different criteria: i) winter, based on high sea ice concentration (defined in section 3.3.3), ii) continuous periods with significant positive correlation (Fig. 4.8), iii) summer based on low sea ice concentration, and iv) continuous periods of negative correlation. By doing this, we can study if there is a difference between correlation in summer and winter on a larger area than just in the SB-box, and if the correlations in these maps indicate a similar tendency as our correlation time series from the SB-box.

In agreement with the time series, correlation maps from periods with high sea ice cover are similar to correlation maps from periods with positive correlation (Fig. 4.10). In both these cases, the highest correlation is found south of the shelf break, east of UIB3, in the

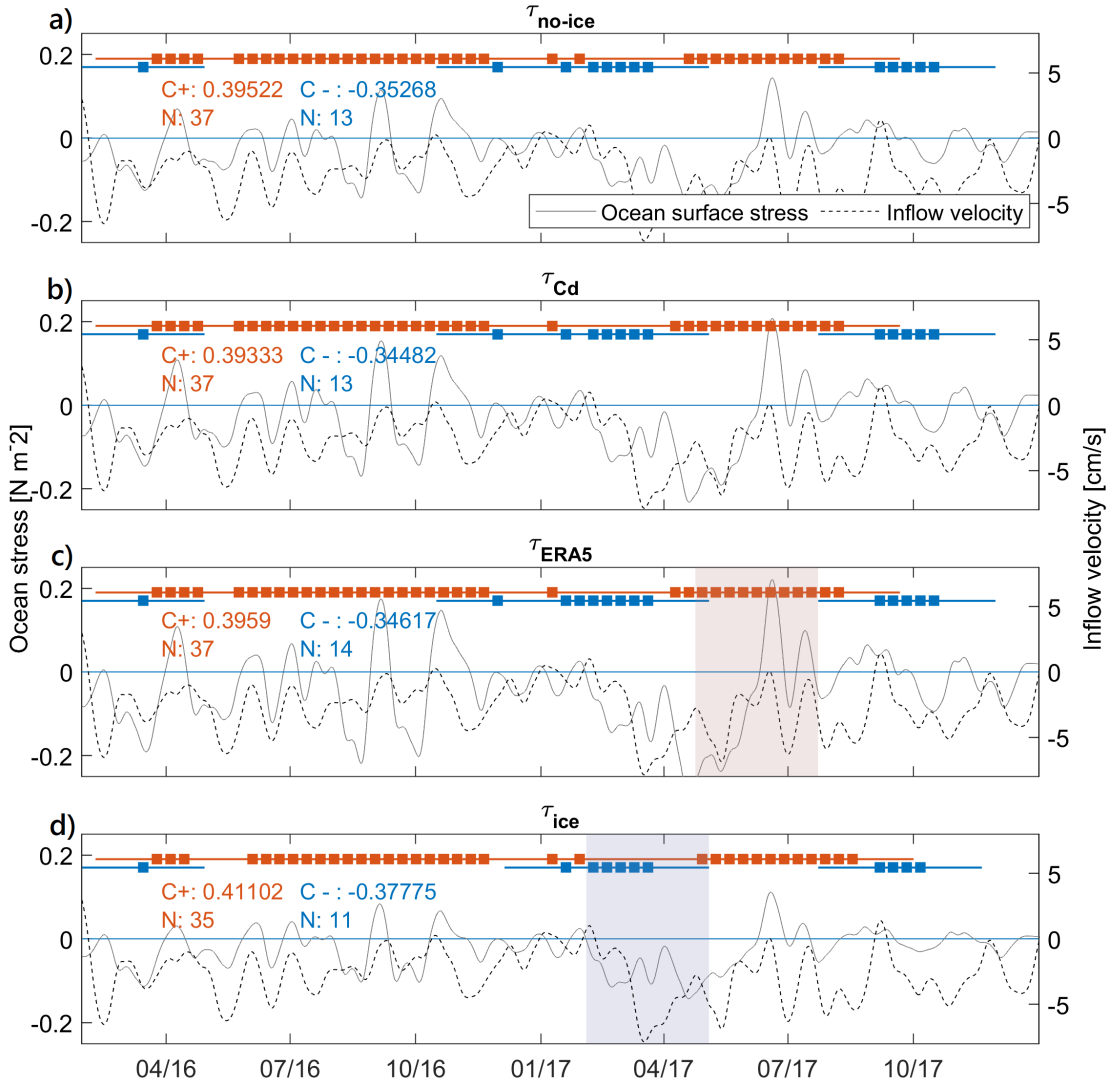

Figure 4.8: Time series and correlation between the along-slope velocity observed at UIB3 and the ocean surface stress based on calculations of ocean surface stress using a) τ_{no-ice}, b) τ_{Cd}, c) τ_{ERA5} and d) τ_{ice}. The respective filtering for the time series and the correlation, and the definition of the red and blue bars are same as in Fig. 4.5. The windows of high negative and positive correlation shown in Fig. 4.9 are indicated by the pale blue and red boxes, respectively.

general location of the Amundsen Sea Polynya (e.g. Yager et al., 2012; Arrigo, 2003). This is the same area as we find the highest correlation for the entire time series. When selecting periods based on high SIC (case i), the highest correlation is $r = 0.42$ (lag = 16h), while when selecting periods of significant positive correlation (case ii), the maximum correlation

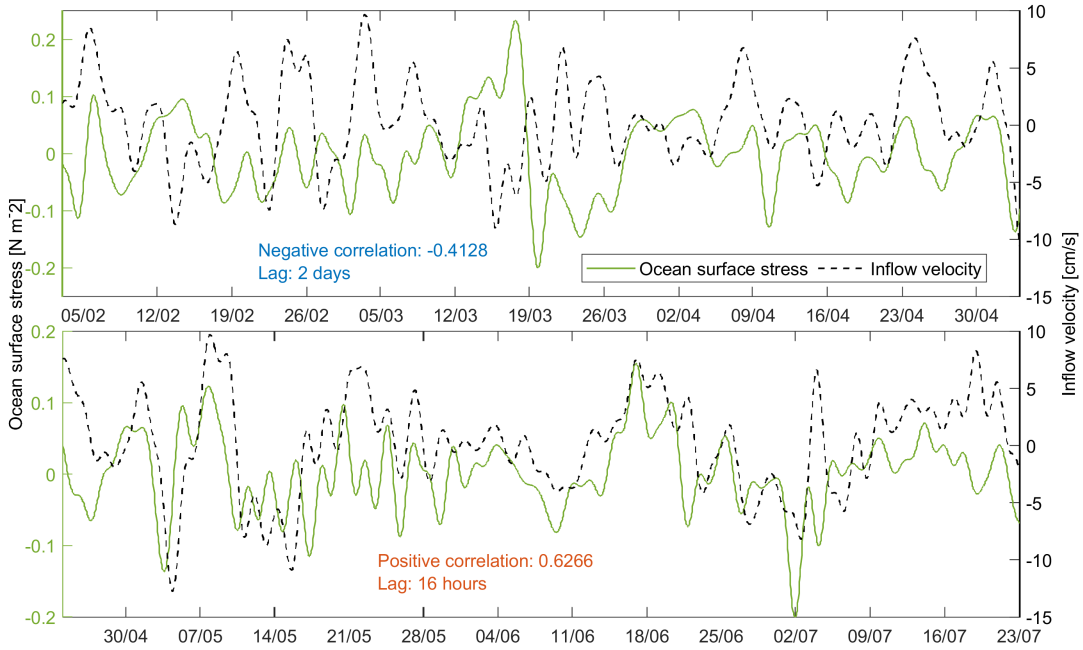

Figure 4.9: An example of bandpass filtered (2 days to 4 months) time series of the ocean surface stress, τ_{ice}, (green line) and the inflow velocity (dashed, black) during a window with high a) negative correlation, and b) positive correlation.

is $r = 0.51$ (lag = 15h) (Fig. 4.10).

During summer, there is no significant correlation unless a longer lag than seven days is allowed. When selecting periods of negative correlation in the SB-box time series, there is significant correlation, but the values are in the range of $r = -0.1$ and $r = 0.06$. Only two small patches that have significant correlation.

τ_{ice} is not resolved along the coastline, and has limitations when the sea ice cover is close to 100% (section 2.5.3). We therefore estimate and compare the correlations using ERA 5, which covers the coastal areas, to see if the improved data coverage along the coastline leads to different results. We find that the difference is very small. In winter we find nearly the same areas of significant correlation, and the areas of high and low correlation generally match. The maximum correlation when using ERA 5 is however slightly lower ($r = 0.48$ compared to $r = 0.51$). This agrees with the time series of correlation when comparing the different methods for calculating ocean stress (Fig 4.8). For the summer months, the correlation is still very low when correlating inflow to ERA5, and the area that is insignificant is much larger compared with the area of significant correlation. The only significant patch that appears, is a slightly negative correlation at the shelf break, north of UIB3.

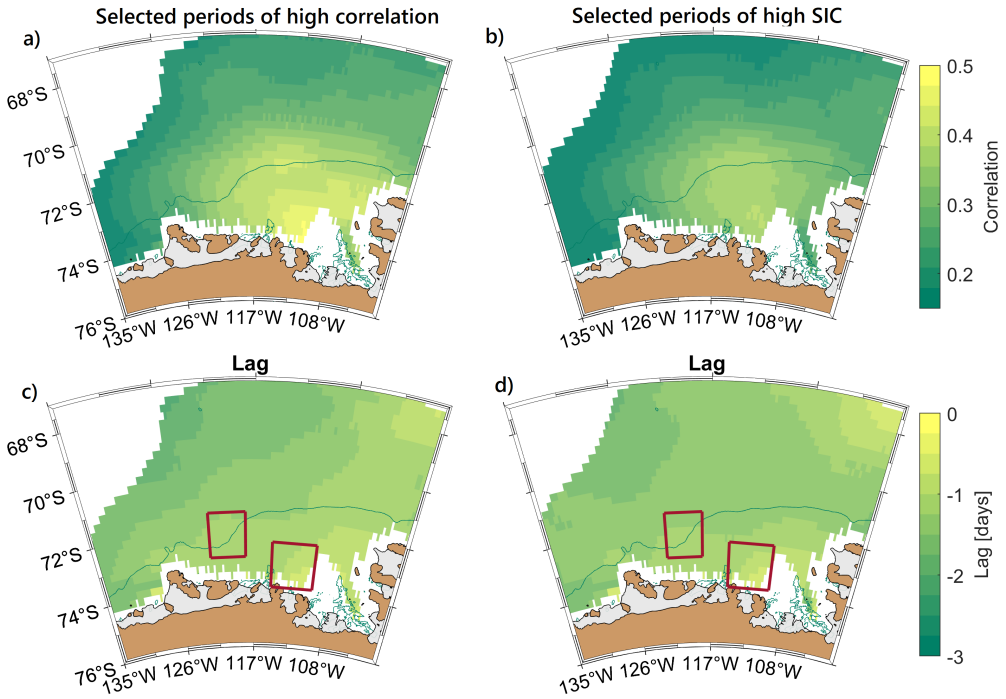

Figure 4.10: Correlation between τ_{ice} and the inflow velocity observed at UIB3 during a) the selected periods of high correlation and b) the selected periods of high sea ice concentration. The lag for the respective periods is shown in c) and d). The SB-box and the eastern-box are marked in red.

The maps of correlation tell us where the highest correlation is found, but as the correlation changes over time in the SB-box (Fig. 4.8), we study the temporal variation in correlation in the area with the highest correlation as well. We refer to the box in the area with the highest correlation as the eastern-box (Fig. 4.10), and compare the correlation in the SB-box to the eastern-box (Fig. 4.11).

We find that the time series of correlation in the zonal direction over the two boxes are similar to each other. The correlation during the positive periods in the eastern-box is higher, on average $r = 0.45$, $N = 38$, compared with $r = 0.41$, $N = 35$ in the SB-box. The negative correlations are weaker, and the SB-box actually has the stronger correlation in this case, with $r = -0.38$, $N = 11$, relative to $r = -0.35$, $N = 9$ for the eastern-box. Both boxes show the pattern of positive correlation in winter and negative correlation in summer. Because of the strong meridional components in the wind field over the eastern-box, we note that the correlation between the meridional ocean surface stress over this box and the along-slope velocity at UIB3 is always negative ($r = -0.35$, $N = 26$), while at the SB-box the correlation is sporadic (positive: $r = 0.33$, $N = 7$ and negative: $r = -0.3$, $N = 19$) (not shown).

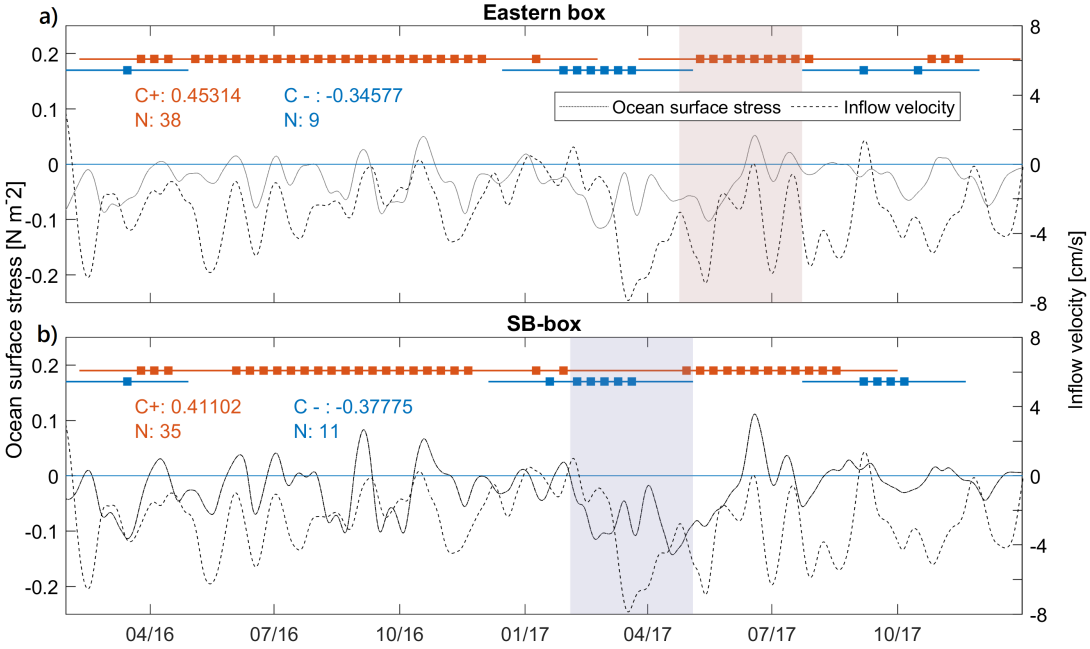

Figure 4.11: Correlation between the inflow velocity past UIB3 (dashed line) and the surface ocean stress (solid line) in the a) u-direction in the eastern break box, b) u-direction in the SB-box, c) v-direction in the eastern box and d) v-direction in the SB-box. Colors and bars denote the same as in Fig. 4.8, and again positive and negative correlation and the number of significant periods are indicated.

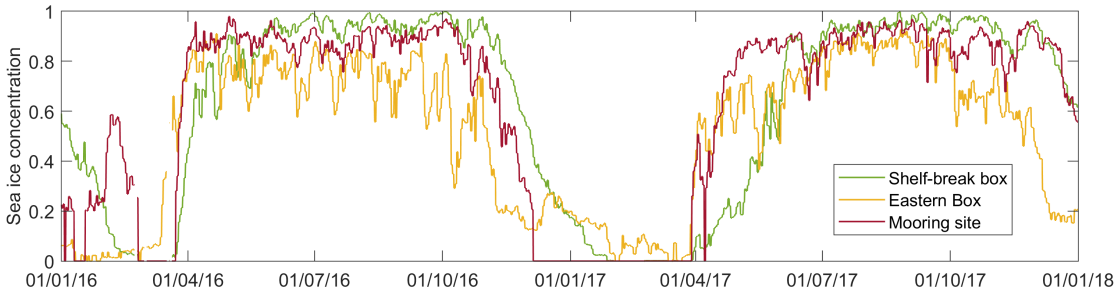

Figure 4.12: Sea ice concentration averaged over the SB-box (green), the eastern-box (yellow), and the mooring site (red). Between 22. February and 21. March the data set has four spikes that have been removed.

4.7 Spectral analysis of ocean surface stress and the along-slope velocity

To investigate why the wintertime correlation at the eastern-box, with almost no lag, is stronger than in the SB-box, we compare the ocean surface stresses in these boxed using spectral analysis and coherency analysis. If their respective frequency spectra have peaks at different periods, this could be a likely explanation for the difference we see in correlation. We study the power spectral density for three separate time periods: i) the entire period, ii) winter, and iii) summer, for periods of 1.5 to 20 days.

The power spectral density (PSD) of the ocean surface stress averaged over each of the two boxes have similar distributions of energy, with no major peaks on any periods (Fig. 4.13). For all three cases, the ocean surface stress in the SB-box generally has higher PSD on periods longer than two days, while on shorter periods the difference between the two boxes is small. There is an exception during summer for a period range around four days where the two boxes have the same PSD.

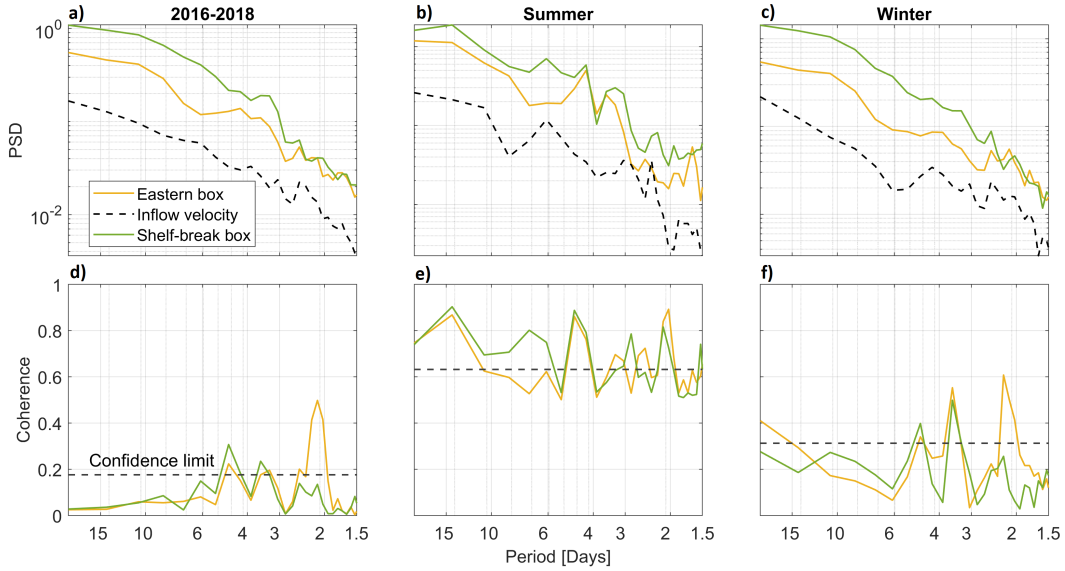

Figure 4.13: Upper panel: frequency spectra for ocean surface stress in the eastern-box (yellow), SB-box (green), and the along-slope velocity observed at UIB3 (black, dashed). Lower panel: coherence comparing the along-slope velocity past UIB3 with the ocean surface stress in the eastern-box (yellow) and the SB-box (green). The confidence limit is marked in the coherence spectra with the black dashed line. NFFT: 1024. a, d) the entire period, b, e) summer, c, f) winter.

Spectra of coherence between ocean surface stress from each of the boxes with the along-slope velocity observed at UIB3, enables us to identify frequencies that are important in both time series. Any differences between these two coherence spectra might give an

indication of periods of variability that are important for the differences in correlation of the two boxes with the along-slope velocity. (section 2.6.2 and 3.4.3).

For the time series as a whole, there is a clear peak in coherence between the eastern-box and the inflow velocity above the confidence limit at the 2-day period. The summer spectra is more complex due to fewer DOFs (section 3.4.3), but peaks at 3 and 6-10 days appear for coherence of the inflow velocity with the SB- and not the eastern-box. In agreement with the spectra for the entire time period, there is a peak at about 2 days in winter for the eastern-box and not the SB-box. The similarity between the winter spectra and the spectra for the entire time period agree with what we find based on the maps of correlation.

4.8 Variability in ocean surface stress and Ekman pumping velocity following the SAM-index

In analogy to looking into the ocean surface stress and resulting Ekman pumping velocity during the seasons (section 4.5.1), we briefly study periods of high and low SAM because of the large difference in the wind field during S16 and S17, and the high SIC during S16. The SAM-index is mostly positive throughout S16 and W16, negative during S17, and positive during W17 (Fig. 3.5). The characteristics of the SAM-index during 2016-2018 fall within the general expectation (section 2.4): the mean is positive in accordance with the overall trend, it has variations on both short and longer timescales, and the absolute values are well within the $\pm$ 6 interval.

The 2016-2018 mean ocean surface stress and Ekman pumping velocity, and the ensemble averages for periods of positive and negative SAM is shown in Fig. 4.14. Compared to the seasonal distribution of ocean surface stress and Ekman pumping (Fig. 4.7), the mean ocean surface stress is similar to S16, while the ocean surface stress during positive SAM is similar to the average winter situation. The ocean surface stress during negative SAM does not have the same apparent similarities to S17, which contradicts what might have been expected. The zero-contour does shift north during negative SAM in agreement with the definition, though not nearly as far north as during S17.

Maximum eastwards ocean surface stress is found during positive SAM (0.12 N m^{-2}, relative to 0.11 N m^{-2} during winter), while the maximum westwards ocean surface stress is about -0.08 N m^{-2} for all cases (relative to the overall seasonal maximum of -0.11 N m^{-2} during S16). The mean ocean surface stress is westwards during negative SAM and eastwards during positive SAM.

Positive vertical velocities are strongest during positive SAM (0.24 m/day), while the negative velocities are strongest during negative SAM (-0.10 m/day). The spatial distribution of positive and negative vertical velocities have the same similarities to the seasons as

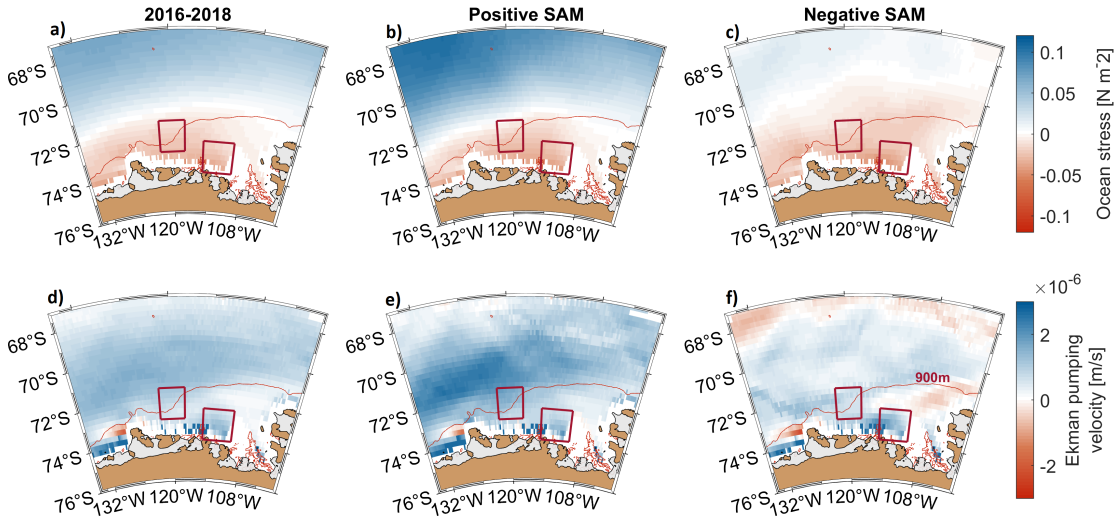

Figure 4.14: Mean ocean surface stress (upper panels), and Ekman pumping velocity (lower panels) over a, d) 2016-2018 c, d) positive SAM, and e, f) negative SAM. Note that the limits of the color scale is the same as in Fig. 4.7. The SB-box, eastern-box, and the 900 meter isobath (red line) are included.

the ocean surface stress. The mean is similar to S16 except that the high positive velocities on the continental shelf and shelf break in the regions near the SB- and eastern-box are not found. Vertical velocities during positive SAM are strong in the region of the zero-contour in ocean surface stress, similarly to the winter-mean. Finally, during negative SAM, there is an increase in vertical velocities on the continental shelf in the eastern-box, there is an area of negative velocities to the east along the shelf break, and aside from this, the velocities are generally weak, all in agreement with the situation during S17.

Chapter 5

Discussion

We present new data from a moored array (UIB3) near one of the many fronts of the Getz Ice Shelf (Fig. 5.1). We describe the general characteristics and variability in hydrography and circulation in the UIB3-trough, and study possible drivers of this variability. These are all aspects that have not previously been studied in detail at this location. Due to the proximity of the mooring to the ice shelf, and reported high melt rates in the Amundsen Sea, we pay special attention to processes that might impact the heat content and heat transport at UIB3. We are inclined to think that the variability in these two features are driven by different processes, as the heat transport, which is closely connected to the current towards the ice shelf at UIB3, correlates relatively well with the ocean surface stress, while the heat content does not. We therefore discuss the correlation related to heat transport and ocean surface stress first, and then possible drivers of heat content, with a focus on its interannual variability, and pathways that may bring mCDW to UIB3. We then discuss the local circulation in the UIB3-trough, and finally possible errors in our estimations of ocean surface stress.

5.1 Geographical variations in correlation

The correlation between the ocean surface stress and the current towards the ice shelf at UIB3, the along-slope velocity, varies geographically. Previous studies from the Siple trough have found high correlation between atmospheric forcing in shelf break regions, and variability near the ice shelf (Assmann et al., 2019). This is not what we find. The correlation is mostly significant during winter, and the highest correlation is found east of UIB3 (Fig. 4.10), in the Amundsen Sea Polynya region (Fig. 5.1). Based on these results, we selected two regions: one at the shelf break (SB-box), where we expected high correlation, and one where we found the highest correlation (eastern box), (Fig. 4.10). We

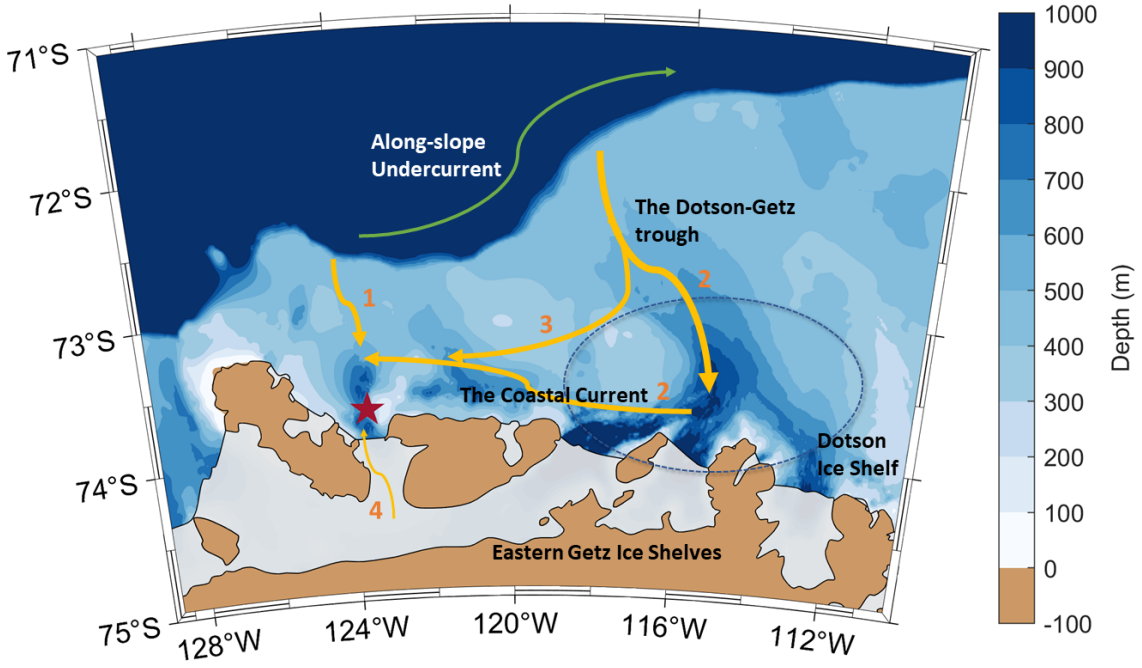

Figure 5.1: Schematic of the discussed pathways that may bring mCDW to the UIB3-trough. The dashed circle indicates the general location of the Amundsen Sea Polynya, and the red star is the location of UIB3. The green arrow indicates the eastward along-slope undercurrent.

discuss processes that may induce this spatial distribution in correlation between ocean surface stress and along-slope velocity at UIB3.

The variability in ocean surface stress is similar in the two boxes (Fig. 4.13) for most periods above one day. The exception is at the two-day period during winter, where there is a significant peak in coherence between ocean surface stress in the eastern box and the along-flow current. This peak does not appear in coherence between the SB-box and the along-flow current, and might therefore be important for the high correlation in the eastern box.

The eastern box is influenced by strong katabatic winds, while the SB-box is located further away from the coastline, and is less influenced by these winds (Fig. 4.4). It seems likely that the zonal winds over the SB-box and the generally stronger, south-easterly, winds over the eastern box induce different dynamical processes. The higher correlation between

along-slope velocity with meridional ocean surface stress over the eastern box compared with the SB-box (not shown) supports the notion that the meridional component might be one of the features responsible for the location of high correlation.

The coinciding locations of the eastern box and the Amundsen Sea Polynya (Fig. 4.10 and 5.1) is possibly a key factor for the overall location of the highest correlation. Sea ice concentration (SIC) is included in our parameterization of ocean surface stress, and the difference between the SIC in the two boxes is notable (Fig. 4.12). We find that SIC in the eastern box is lower, but varies more strongly within the seasons compared to the SB-box. High SIC generally dampens the momentum flux into the ocean (e.g. Martin et al., 2016), so a possibility is that the lower SIC in the eastern box during winter means that the wind field in the eastern box has a higher influence on dynamical processes than in the SB-box.

The coastal current flows westwards through the Amundsen Sea Polynya, and later passes regions near the UIB3-trough (Fig. 2.3). Processes that influence the properties of the coastal current may in turn influence properties in the UIB3-trough through advection. Kim et al. (2016) observe a seasonal signal in the strength and baroclinicity of the coastal current in the Amundsen Sea Polynya. They relate this seasonal signal to gradients in sea surface height induced by the ocean surface stress along the coast, and to variability in the stratification in the polynya, which both act to change the depth of the pycnocline. Such forcing may lead to variability in the relative strength of barotropic and baroclinic responses in the coastal current. Barotropic movement is more bounded by the topography than baroclinic movement, and a seasonal signal in the baroclinicity of the coastal current may therefore imply seasonal variability in the pathway of the coastal current. Shifts in the coastal current pathway may impact UIB3. Since both the strength and the baroclinicity seem to be influenced by the ocean surface stress in the eastern-box, and since the response to this forcing will travel as a Kelvin wave westward along the coast, this may be part of the explanation for both the observed high correlation and the short lag of $\sim$ 15h.

The 15-hour lag, and the approximately 230 km between the eastern-box and UIB3, means that any change in the along-slope velocity directly induced by the ocean surface stress would have to travel quickly. We estimate an average depth of 500 m (Fig. 2.1), which gives a velocity for a shallow water wave of 70 m s^{-1}, and an advection timescale of less than one day. It is therefore possible for a signal induced by the ocean surface stress in the eastern-box to propagate with a Kelvin wave to the UIB3-trough in less than a day, and eventually induce a response at here.

Further studies of the coastal current in the Amundsen Sea Polynya may improve our understanding of the connections between the seasonal signal in the coastal current, and the variability of the along-slope current in front of the Getz Ice Shelf. The mooring used in the study by Kim et al. (2016) was operative in 2016-2018, so if these data were made available, direct comparison between observations from UIB3 and this mooring would be possible. Inspection of data from a regional model would also be useful.

5.2 Temporal variations in correlation

We find significant correlations between the ocean surface stress and the along-slope velocity at UIB3 throughout the mooring period. The correlation shifts between positive and negative values (Fig. 4.8 and 4.11), which indicates that the dynamical mechanisms that connect the ocean surface stress to the circulation in the UIB3-trough vary throughout the mooring period. Since the alternating correlation tends to follow periods of high and low SIC during 2016 and the first half of 2017, it seems possible that the shift in dynamical processes is driven by seasonal variability.

Our results indicate that the SIC itself is not the main driver for the alternating correlation because of three features. Firstly, correlation of the along-slope velocity with the ocean surface stress without including the effect of SIC, τ_{no-ice}, gives the same pattern as when including SIC (Fig. 4.8). Secondly, in the eastern-box at the center of the Amundsen Sea Polynya, the pattern is also the same (Fig. 4.10). If the large differences in SIC between the seasons were responsible for a change in dynamical processes, it seems likely that the pattern would also differ more between the eastern-box and the SB-box. Thirdly, although there is no large change in SIC in the middle of W17, the pattern does not hold throughout the mooring period. This last argument does not rule out a general seasonal dependency. It is possible that the correlation usually varies seasonally, but that processes during W17 were influenced by other features that disrupted the positive correlation. The short time series hinders us from drawing conclusions regarding this, though we do not find evidence of abrupt changes during W17.

The seasonality and variability in the large-scale wind field, ocean surface stress, and resulting Ekman pumping could also influence the observed temporal variability in correlations (Fig. 4.4 and Fig. 4.7). The SB-box is however more strongly influenced by such seasonality than the eastern-box, through the position of the ASL, the SAM, and the latitude where the zonal wind changes direction (the zero-contour). As we find similar alternating correlation in both boxes, seasonality in dynamics induced by the large-scale wind field and ocean surface stress is not a likely explanation either.

The observed seasonal signal in strength and baroclinicity of the coastal current (section 5.1, and Kim et al., 2016) could possibly explain the alternating correlation. There is however no evidence that the wind field over the SB-box has a connection to variability in the coastal current, so this suggestion fail in explaining the alternating correlation at the shelf break.

Overall, our results call for further investigation of possible drivers of dynamical processes that may be responsible for the alternating correlation between ocean surface stress and along-slope velocity. An extended time series might indicate whether this seemingly seasonal alternation is the mean state of correlation between these variables, or whether the

alternation is a feature specific for the mooring period. This would be helpful for the general understanding of important dynamics in the region, and possibly give further insight in the drivers of the correlation.

5.3 Heat content

There is no pronounced seasonal signal in the heat content at UIB3, but an interannual variation: the highest heat content is found towards the end of 2016, and the lowest towards the end of 2017. The evolution in heat content generally co-vary with both the temperature and the thickness of the warm layer, and the lack of a seasonal cycle in these two parameters agree with results from the Siple trough (Assmann et al., 2019). We first discuss possible drivers of the variability in heat content, and then pathways that might bring mCDW to UIB3. The main pathways we consider are summarized in Fig. 5.1.

5.3.1 Drivers of the interannual variability

The observed interannual variability in heat content may be related to the ocean surface stress. Previous studies suggest several sources of on-shelf heat variability, such as: wind forcing and ocean surface stress, ocean dynamics and the eastward undercurrent, eddies and tides, far field drivers of heat variability within the CDW, and Kelvin waves propagating along the continental slope (Dotto et al., 2019, and references therein). Not all these drivers have been assessed in direct relation to the Amundsen Sea, such as eddies and tides, so the importance of these processes in the Amundsen Sea are unclear. Ocean dynamics, on the other hand, have been looked into, and Dotto et al. (2019) show that the along-slope eastward undercurrent (green arrow in Fig. 5.1) can be forced to flow on-shelf along different pathways, depending on the shelf break topography. Wåhlin et al. (2012) suggest that the undercurrent may lead to lifting of the thermocline through bottom Ekman transport, which allows water masses previously located deeper than the continental shelf to flow onto the shelf.

Local forcing of the heat content through processes such as convection, may also be important. During S17, there was no sea ice at the UIB3 mooring site for several months, and leading up to W17, the open water refreezed rapidly (Fig. 4.12). There is evidence of deep mixing and ventilation of WW around October in both years, though the period lasted longer in 2017 (Fig. 4.1), which may be related to the long period of open water during S17. The end of the period where WW is present in 2016 overlaps with the start of the overall warmest period, while in 2017, WW is present when the layer of warm water is also thin. These different combinations of the thickness of deep warm water, and the local forcing of the cold overlying layer, influence the variability in heat content: although WW

is present during both years, the heat content is much lower by the end of 2017 (Fig. 4.5).

During summer 2015 (prior to the mooring period), the wind field was similar to S17, with a broad band of easterlies over the shelf break, which agrees with what we expect during summer. The wind-field during S16 does not agree with the expected summer wind-field: the zero-contour was shifted south to latitudes usual for winter, and the westerlies had similar strength to W16 (Fig. 4.4). This large difference between the two summers might be tied back to variability in the SAM. When the SAM-index is positive, the westerlies increase in strength and shift south (Thompson et al., 2011), and the spatial coverage of sea ice tend to increase (Lefebvre and Goosse, 2005). When the index is negative, the situation is reversed (section 2.4). This agrees with the differences we find between the two summers. During S16, the SAM-index is mostly positive, the westerlies have shifted far south (Fig. 4.4), and SIC is relatively high (Fig. 4.12). During S17 the index is mostly negative, the westerlies have shifted northward, and the period of low SIC is much longer.

The winter of 2015, preceding the mooring period, had stronger westerlies than both W16 and W17. It seems likely that the three consequent seasons of persistent westerlies (winter of 2015, S16 and W16) might have had an influence on the interannual and large-scale features of the cumulative Ekman pumping anomaly and the undercurrent at the shelf break. The difference in cumulative Ekman pumping anomaly (Fig. 4.6) and Ekman pumping velocity (Fig. 4.7) between S16 and S17 supports this notion.

Variability in the Ekman pumping at the shelf break could affect the heat content at UIB3. Strong positive gradients in the ocean surface stress lead to upward Ekman pumping, and lifting of the thermocline. If the lifting of the thermocline is substantial, it might reach above shelf break depth. In areas west and east of UIB3, where the shelf break is much deeper than the 460 m north of UIB3, the thermocline is often located above shelf break depth, allowing a continuous flow of CDW on-shelf. The varying volume of CDW allowed onto the continental shelf is reflected in the Ekman pumping anomaly, which determines the thickness of the CDW-layer near the ice shelves, such as west of Siple Island where the shelf break is about 570 meters deep (e.g. Assmann et al., 2019). The variability in heat is therefore driven mainly by the volume of CDW that is allowed onto the shelf, not whether it is allowed onto the shelf or not.

The spatial distribution of seasonally averaged Ekman pumping velocities over the Amundsen Sea (Fig. 4.7) cannot be directly translated into lifting or depression of the thermocline, as this is a cumulative effect. We can however infer that the high positive velocities during S16, W16 and W17, relative to S17, may have acted to lift the thermocline over a large area, which agrees with the time series of Ekman pumping anomaly we see in the SB-box specifically (Fig. 4.6). However, the thermocline tends to deepen towards the west (Dotto et al., 2019). This deep thermocline, in combination with the shallow shelf break north of UIB3, means that the thermocline would have to be lifted higher to let warm water onto the shelf here, compared with locations further east and west. The fact that we find

unmodified CDW off-shelf at shelf break depth in the CTD-profiles from 1994, 2000, and 2007 (Fig. 4.2 and 4.3), and not in the profiles obtained at the mooring-site may indicate that i) the ASF generally intersects the slope below the shelf break, ii) efficient mixing takes place at the shelf break, or during transport southwards across the continental shelf, iii) there is no direct path between the shelf break to the north and UIB3, in agreement with indications from the bathymetry (IBCSO), or that iv) mCDW at the mooring-site does not originate from the shelf break directly north of UIB3.

We cannot estimate the advection timescale for warm water at the shelf break to reach UIB3 with certainty, due to the lack of current-data on the continental shelf. Consequently, we cannot assess the suggested mechanisms that hinder CDW from reaching the UIB3-trough with certainty either, as the CTD-profiles only give information at one specific time. CTD sections across the shelf break would be useful to determine the average position of the thermocline, and to estimate the required ocean surface stress to lift the thermocline above the shelf break. During the mooring period, the ocean surface stress at the shelf break and the heat content does however have shorter periods of sporadic correlation ($r = 0.37$, $N = 12$). Shelf break processes, and possibly Ekman pumping, might occasionally influence the variability in heat content at the mooring site. This was the case for the Western Amundsen Sea in 2010-2013 (Wåhlin et al., 2013). However, because the Ekman pumping anomaly at the shelf break, and heat content at UIB3 do not co-vary (Fig. 4.6 and Fig.4.5), it seems unlikely that the general variability in heat content at UIB3 is driven by lifting of the thermocline through Ekman pumping alone.

Dotto et al. (2019) study heat content variability on the Amundsen Sea continental shelf, and find that their eastern and western study areas have different drivers of variability, but they relate both processes to variations in the along-slope undercurrent. Their eastern area (leading up to Pine Island and Thwaites Ice Shelves, Fig. 2.1), is characterized by a deep shelf break, similar to the roughly 570 m deep shelf break leading to the moorings west of Siple Island (UIB1 and UIB4), where CDW has constant access into the trough. Their western area (the Dotson-Getz trough, Fig. 2.1) has a shallower shelf break (about 520 m), and here, they find that CDW does not have constant access onto the shelf. They find that an increase in heat content in the Dotson-Getz trough is driven by the lifting of isopycnals at the shelf break, which in turn is forced by wind driven intensification of the undercurrent. In contrast to Dotto et al. (2019), we do not find evidence of co-variance between heat content and the ocean surface stress. This suggests that although the Dotson-Getz trough and the shelf break north of UIB3 have similarities, the difference in shelf break depth and thermocline depth may be too large for the two regions to be directly comparable.

Another possible driving mechanism for inflow of warm water to UIB3 is a weak slope front, and consequently a weak undercurrent (Walker et al., 2013). The seasonal wind field is important for inducing, and further maintaining the undercurrent (section 2.3, and e.g. Assmann et al., 2013). It is possible that the lack of easterlies during S16 may have relaxed the slope front and weakened the undercurrent during the start of the mooring period, thus

allowing warm waters on-shelf below the relaxed ASF (Fig. 2.4). During the second half of the mooring period, local convection connected to low SIC during S17 (Fig. 4.12) may have ventilated and cooled the upper 440 meters of the water column at UIB3. At the same time, the broad band of easterlies during S17 (Fig. 4.4) may have contributed to a strengthened slope front and slope currents, again hindering warm, dense water to flow onto the shallow continental shelf.

5.3.2 Possible pathways of "warm" water

We discuss four pathways that may bring mCDW to the UIB3-trough (Fig. 5.1). mCDW may flow over the continental shelf from the shelf break north of UIB3 (pathway 1), flow onto the continental shelf through the Dotson-Getz trough and either follow the coastal current towards UIB3 (pathway 2), or veer westwards before reaching the ice shelves (pathway 3), or mCDW may originate from passages under the ice shelf south of UIB3 (pathway 4, discussed in section 5.4).

Pathway 1 may bring mCDW to UIB3 from the shelf break north of UIB3, at about 124°W where the western on-shelf CTD-profiles are obtained (Fig. 3.1). Although the shelf break is shallow here, and the thermocline likely is deep (Dotto et al., 2019), the warmest water at UIB3 (0.13°C, Fig. 4.2) corresponds to temperatures found in the front that separates WW from CDW at the shelf break (Fig. 4.3). The western on-shelf CTD-profiles have 0.5° higher maximum temperatures than the on-shelf profiles taken further east (Fig. 4.3), which agrees with results from a model run by Nakayama et al. (2014) over the period 1984-1998.

The presence of the ASF is reflected in the high temperatures off-shelf, relative to on-shelf at shelf break depth, but as discussed in section 5.3.1, the ASF vary in strength, which means that this may not always be the case. However, we have to be careful when using differences in maximum temperature at the shelf break in our argumentation. Horizontal shifts in the slope front location lead to large changes in bottom temperatures since the thermocline is depressed all the way to the bottom. Such horizontal shifts in the slope front location might result from e.g. tides or shelf waves across the shelf break (e.g. Semper and Darelius, 2017). However, the tidal currents in this region are low (Padman et al., 2018, 2002). In the currents produced by the numerical model study (averaged over 2011-2012) described in section 2.1 (Fig. 2.3 and Assmann et al., 2013), there is however no indication of this suggested pathway. We note that the currents from this model suggests a relatively strong current northward on both sides of the UIB3-trough at 450 m depth, just north of the ice shelf. This does not correspond to the mooring observations, and we can therefore not fully rely on the currents from this model. As a consequence we do not completely rule out pathway 1 as a possibility.

Warm water could also access the UIB3-trough trough pathway 2 and 3 along the continental shelf to the east (Fig. 5.1). The shelf break leading to the Dotson-Getz trough is slightly deeper than the shelf break north of UIB3, and warm water is observed to flow onto the shelf through this shallow trough (section 5.3.1 and e.g. Dotto et al., 2019; Nakayama et al., 2014; Wåhlin et al., 2010). Warm waters may thus flow onto the central shelf through this trough, and find a way towards UIB3 downstream of the shelf break. mCDW may either follow the trough all the way to the Dotson or Eastern Getz Ice Shelf, and then follow the coastal current westwards (pathway 2), or to find an opening westward earlier on, and veer towards UIB3 before reaching the ice shelves (pathway 3). The lack of meltwater at UIB3 (Fig. 4.2) may give some indications of which pathways are most likely. When assessing these possibilities, we need to keep the uncertainty of the bathymetry in mind.

Pathway 2 along the coastal current should imply that the water masses at UIB3 have been in contact with water masses from areas near the ice shelves to the east. Deep warm water masses from these areas tend to contain meltwater, and therefore align with the Gade-line (Wåhlin et al., 2010). We observe little evidence of meltwater at UIB3 (which we discuss further in section 5.4), and this pathway is therefore not very likely.

Pathway 3 is more likely, due to the absence of meltwater at the mooring-site. Kalén et al. (2016) find that the circulation in the Dotson-Getz trough is mostly cyclonic, but in their observations from 2008, the bottom current at the western side of the trough (about 400-550 meters depth) flows southward with temperatures above 0°C. This is not observed in 2010. We do not have data at the UIB3-trough from 2008 or 2010 for comparison with the variability in heat content during 2016-2018, and due to inaccuracy in the bathymetry, we do not know if the observed warm water below 400 m depth has access to the mooring-site. However, if there is such a pathway below 400 m depth, the warm current observed in 2008 might have reached the UIB3-trough, and a similar situation may have occurred in 2016. We note that the results from Dotto et al. (2019) support a similar argument. There seem to be mostly cold water between the mooring site and the warm inflow in the Dotson-Getz trough, but their results from a model-study (averaged over 2000-2014) also suggest a weak current towards south-west, with temperatures above 0°C. As this is the long-term mean, this weak on-shelf bottom current is fluctuating, with periods of higher current speeds. If water at UIB3 circulates in the trough for longer time periods, as we suggest in section 5.4, episodic flow of warm water into the trough is sufficient to sustain a relatively warm bottom layer in the UIB3-trough.

5.4 Circulation in the UIB3-trough

We mention in section 5.3.2 that the modelled currents averaged over 2011-2012 (Assmann et al., 2013) does not correspond properly to observed currents past UIB3. We therefore discuss mechanisms of circulation, and the possibility of recirculation in the UIB3-trough.

Melting of ice shelves in a trough can set up a cyclonic current in and out from under the ice shelf (e.g. Holland, 2017). In the case of a defined and bounded trough, such as the UIB3-trough (IBCSO, Fig. 3.2), this may create a recirculation system within the trough. If the inflow past UIB3 cause melting, some of our data points should be aligned with the Gade-line in the TS-diagram (Fig. 4.2), similarly to what Wåhlin et al. (2010) find in the Dotson-Getz trough. In the case of recirculation in the trough, we might expect to see meltwater in all profiles, while if there is no recirculation we should see meltwater in only the western profiles from 2000 and the seal-profiles. We do not observe alignment with the Gade-line in the TS-diagram, for any of the hydrographic profiles, or for the UIB3-data. This probably means that the layer of mCDW is not thick enough to reach the ice shelf base south of UIB3. The warmest temperatures observed in this study are from the seal in 2014 (Fig. 4.3). Since these profiles do not indicate meltwater, this is a strong indication that meltwater is not generally present in the UIB3-trough.

Alternative pathways underneath the ice shelf (illustrated by pathway 4 in Fig. 5.1) may, however, connect the UIB3-trough to other fronts of the Getz Ice Shelf (Jacobs et al., 2013). In this case, inflow past UIB3 may still induce melting, if the meltwater-mixture flows out the trough through channels underneath the ice. Such pathways could also be a source of mCDW, but if this was the case, meltwater would likely be part of the mixture. The similarity between the 2000-profiles in the trough do however indicate recirculation, although 2000 was an exceptionally cold year in the Amundsen Sea (e.g. Assmann et al., 2019), which suggest that even though these two profiles are similar to each other, this may not be the general case. The similarity between the seal-profiles below about 500 m, and the decrease in gradients in the profiles throughout the summer season (Fig. 4.3, Table 3.2) supports the argument on recirculation. Further, the differences between the seal-profiles at shallower depths could indicate differences between the northern and southern part of the UIB3-trough.

The presence of meltwater in the upper layers of the water column cannot be inferred from a TS-diagram alone, but require additional variables such as oxygen or helium (e.g. Schlosser et al., 1990). However, if meltwater is in fact not generally present, the apparent recirculation must be caused by other processes than meltwater induced circulation. The geometry of the UIB3-trough, and the general situation cyclonic circulation in Southern Hemisphere troughs (e.g. Jacobs et al., 2013) may explain the indications of recirculation in the UIB3-trough.

To end this discussion on the circulation and lack of observed meltwater in the UIB3-trough, we note the roughly estimated upper limit of contribution by the heat transport in the UIB3-trough to the overall melt rate of the Getz Ice Shelf of 0.6 m/year. Considering the average rates of $1.1 - 4.1$m/year found by Jacobs et al. (2013), it seems unlikely that the heat transport past UIB3 induces such a large contribution. This is however a back-of-the-envelope estimation, where we assume that absolutely all the heat transport is used for ice melt, which is an unlikely scenario. We do not know for certain whether the current flows out on the western side of the UIB3-trough, or if channels underneath the ice play an important role, but if the heat transport does in fact reach the ice shelf, some of the heat would probably go into the process of heating the ice, making it unavailable for melting. If the heat transport past UIB3 contributes to ice melt, the rates are therefore likely considerably lower than our estimations.

5.5 Calculations ocean surface stresses

This study is highly dependent on the ocean surface stress parameterization, so we end our discussion by noting possible errors and weaknesses in these parameterizations. We neglect motion of the ocean below the sea ice, which means that in our calculations following Dotto et al. (2018), we assume that the only factors influencing the ocean surface stress are the wind and the ice movement. This implies three main aspects. First, any occurrence of fast ice implies that the ocean surface stress is zero. Second, when assuming an initially still ocean, any movement of ice will add momentum to the ocean. However, if the currents are stronger than the movement of the ice, the transfer of momentum is from the ocean to the ice, meaning that the ice slows the ocean down, even though they are moving in the same direction. Areas with strong currents may therefore show too low magnitude, and potentially even wrong direction of the total ocean surface stress. Finally, the ice and ocean generally have velocities of the same order of magnitude, while the wind is often much stronger. We therefore risk to introduce a larger error when neglecting ocean movement in areas with sea ice than in areas without.

These three aspects suggest that our calculations of ocean surface stress are most correct in areas without a complete sea ice cover, and in areas without strong ocean currents. Estimations of the stress is therefore possibly distorted by the surface slope current in the SB-box, and by the coastal current in the eastern-box. The eastern-box do however coincide with the location of the Amundsen Sea Polynya (e.g. Yager et al., 2012; Stammerjohn et al., 2015) which means that the possibility of negative drag on ocean movement caused by the sea ice is less present here. This does not provide an explanation for the difference in correlation, but it is an indication that our results from the eastern-box might be more physically valuable than results from the SB-box. Acknowledging these possible errors, we include SIC and sea ice motion in our estimation of ocean surface stress due to the fact that other studies have found that it is crucial to include sea ice for a realistic presentation of the

stress, (e.g. Dotto et al., 2018; Martin et al., 2016). At UIB3, the SB-box and the eastern-box, the errors are limited as the variability in SIC is high, but never a full 100%, and as ocean currents are not included in any of our proposed methods, this is not a particular drawback limited to the method following Dotto et al. (2018).

Chapter 6

Conclusions and Outlook

Conclusions
Two years of mooring data is a large contribution to the data basis in the Western Amundsen Sea. Although this time span asserts some limitations regarding the seasonal and interannual variability discussed in this study, we make a few final remarks regarding the hydrography, the circulation, and the drivers of variability in the UIB3-trough. mCDW is present at all times, but as we do not see much evidence of meltwater, the layer is likely too thin to induce melt at the ice shelf base. However, channels underneath the ice shelf could connect the UIB3-trough to other fronts of the Getz Ice Shelf, and transport the meltwater away through passages below the ice shelf.

It is not clear what mechanisms bring mCDW to the mooring site. The three consequent seasons (winter of 2015, S16 and W16) of persistent westerlies, and resulting ocean surface stress, has likely influenced the large-scale processes at the shelf break, such as the strength of the Ekman pumping, the ASF, and the along-slope undercurrent. Ekman pumping seems unlikely as a main driver of variability in heat content, as the heat content and cumulative Ekman pumping anomaly does not co-vary. Instead, a weakening of the undercurrent and the ASF through the lack of easterlies during S16 may be decisive factors for the variability in heat content in 2016-2018. Pathway 3 (Fig. 5.1) may lead mCDW from the Dotson-Getz trough to UIB3, if the bathymetry allows the flow to veer westwards before reaching the Dotson or Eastern Getz Ice Shelves. The IBCSO bathymetry is too uncertain to assess this pathway properly. However, as there seem to be recirculation in the UIB3-trough, the flow of waters above 0°C that occasionally depart from the Dotson-Getz trough and flow towards the south-west, may provide a source of mCDW that helps maintain a layer of warm water at UIB3. We cannot rule out the possibility that mCDW is brought to the mooring site through channels and currents from the south (pathway 4).

In contrast to the heat content, the along-slope velocity at UIB3 has significant correlation with the ocean surface stress throughout the mooring period. This indicates that the variability in heat content and currents in the UIB3-trough have different drivers. The location of highest correlation coincides with the Amundsen Sea Polynya. It seems possible that the observed seasonal signal in strength and baroclinicity of the coastal current may be part of the explanation for the high correlation, as the current flows from the polynya and past the UIB3-trough. The estimated propagation time of a shallow water wave match the lag in correlation of $\sim$ 15h. The dynamical processes responsible for the observed temporal alternation in correlation remains to be explained, but it may be seasonally influenced.

We note again that the time span of this study is not long enough to describe the general state of hydrography and circulation, or seasonal features with certainty. Consequently, many aspects related to the drivers of variability in the UIB3-trough remain unknown. Particularly, as features during 2016 distinguish themselves from the long-term average, the period 2016-2018 does not necessarily represent the general situation in this area.

Outlook

In future studies of the drivers of variability in hydrography and currents in the UIB3-trough, an analysis of the large-scale forcing required to bring CDW to the UIB3-trough would be interesting in relation to features such as the positive trend in SAM. Additional information of the hydrography at the shelf break could give insight in the average depth of the thermocline and the strength of the ASF, and would be helpful when assessing the relative importance of the strength of the undercurrent versus the relaxation of the slope front, and the potential for Ekman pumping to lift the isotherms above the shelf break. If such an estimate is made, together with an estimation of the resulting heat content in the UIB3-trough, it would be interesting to attempt to describe the importance of the generally low temperatures in the UIB3-trough as a buttressing effect in relation to the overall stability of the Getz Ice Shelf.

A further investigation of the peak in coherence between ocean surface stress in the Amundsen Sea Polynya and the along-slope velocity at UIB3 at the two-day period, may also be an important aspect for future studies. Variability at this frequency may provide insight in which dynamics that are responsible for the observed high correlation.

Finally, a comparison of the mooring observations with model results would be useful. A model that can recreate the mooring observations would provide a large temporal and spatial data basis. This could be used to i) assess whether the mooring period represents the general situation in the trough, ii) to look at long-term and seasonal variability, and iii) to investigate the possibility that the alternating correlation does in fact have a seasonal signal. Depending on the spatial resolution of such a model, modelled currents in the trough may give a better indication of the local circulation, which is important for the possibility of passages and currents below the ice shelf.

Bibliography

Andreas, E. L., Horst, T. W., Grachev, A. A., Persson, P. O. G., Fairall, C. W., Guest, P. S., and Jordan, R. E. (2010). Parametrizing turbulent exchange over summer sea ice and the marginal ice zone. *Quarterly Journal of the Royal Meteorological Society*, 136(649):927–943.

Arndt, J. E., Schenke, H. W., Jakobsson, M., Nitsche, F. O., Buys, G., Goleby, B., Rebesco, M., Bohoyo, F., Hong, J., Black, J., Greku, R., Udintsev, G., Barrios, F., Reynoso-Peralta, W., Taisei, M., and Wigley, R. (2013). The International Bathymetric Chart of the Southern Ocean (IBCSO) Version 1 . 0 A new bathymetric compilation covering circum- Antarctic waters. *Geophysical Research Letters*, 40:3111–3117.

Arrigo, K. R. (2003). Phytoplankton dynamics within 37 Antarctic coastal polynya systems. *Journal of Geophysical Research*, 108(C8):3271.

Assmann, K. M., Darelius, E., Wåhlin, A. K., Kim, T. W., and Lee, S. H. (2019). Warm Circumpolar Deep Water at the Western Getz Ice Shelf Front, Antarctica. *Geophysical Research Letters*, 46(2):870–878.

Assmann, K. M., Jenkins, A., Shoosmith, D. R., Walker, D. P., Jacobs, S. S., and Nicholls, K. W. (2013). Variability of Circumpolar Deep Water transport onto the Amundsen Sea continental shelf through a shelf break trough. *Journal of Geophysical Research: Oceans*, 118(September):6603–6620.

Chelton, D. B. (1982). Statistical reliability and the seasonal cycle: comments on "Bottom pressure measurements across the antarctic. *Deep Sea Research Part A, Oceanographic Research Papers*, 29(11):1381–1388.

DeConto, R. M. and Pollard, D. (2016). Contribution of Antarctica to past and future sea-level rise. *Nature*, 531(7596):591–597.

Dotto, T. S., Naveira Garabato, A., Bacon, S., Tsamados, M., Holland, P. R., Hooley, J., Frajka-Williams, E., Ridout, A., and Meredith, M. P. (2018). Variability of the Ross Gyre, Southern Ocean: Drivers and Responses Revealed by Satellite Altimetry. *Geophysical Research Letters*, 45(12):6195–6204.

Dotto, T. S., Naveira Garabato, A. C., Bacon, S., Holland, P. R., Kimura, S., Firing, Y. L., Tsamados, M., Wåhlin, A. K., and Jenkins, A. (2019). Wind-driven processes controlling oceanic heat delivery to the Amundsen Sea, Antarctica. *Journal of Physical Oceanography*.

Dupont, T. K. and Alley, R. B. (2005). Assessment of the importance of ice-shelf buttressing to ice-sheet flow. *Geophysical Research Letters*, 32(4):1–4.

ECMWF (2017). Copernicus Climate Change Service (C3S). *ERA5: Fifth generation of ECMWF atmospheric reanalyses of the global climate . Copernicus Climate Change Service Climate Data Store (CDS), 05/23/2018*.

ECMWF (2018). Climate reanalysis, Retrieved from. *https://www.ecmwf.int/en/research/climate-reanalysis. [Date Accessed: 2019-09-29].*

Fyfe, J. C. and Saenko, O. A. (2006). Simulated changes in the extratropical Southern Hemisphere winds and currents. *Geophysical Research Letters*, 33(6):1–4.

Gade, H. G. (1979). Melting of Ice Sea Water: A Primitive Model with Application to the Antarctic Ice Shelf and Icebergs. *Journal of Physical Oceanography*, pages 189–198.

Gong, D. and Wang, S. (1999). Definition of Antarctic Oscillation index. *Geophysical Research Letters*, 26(4):459–462.

Hersbach, H., Bell, B., Berrisford, P., Horányi, A., Sabater, J. M., Nicolas, J., Radu, R., Schepers, D., Simmons, A., Soci, C., and Dee, D. (2019). Global reanalysis: goodbye ERA-Interim, hello ERA5. *ECMWF Newsletter*, (159):17–24.

Heywood, K., Biddle, L., Boehme, L., Dutrieux, P., Fedak, M., Jenkins, A., Jones, R., Kaiser, J., Mallett, H., Naveira Garabato, A., Renfrew, I., Stevens, D., and Webber, B. (2016). Between the Devil and the Deep Blue Sea: The Role of the Amundsen Sea Continental Shelf in Exchanges Between Ocean and Ice Shelves. *Oceanography*, 29(4):118–129.

Holland, D. M. (2013). The Marine Cryosphere. In *Ocean Circulation and Climate: A 21st Century Perspective*, chapter 16, pages 413–442. Elsevier Science & Technology, 2 edition.

Holland, P. R. (2017). The Transient Response of Ice Shelf Melting to Ocean Change. *Journal of Physical Oceanography*, 47(June):2101–2114.

IOC, SCOR, and IAPSO (2010). The international thermodynamic equation of seawater 2010: Calculation and use of thermodynamic properties. Intergovernmental Oceanographic Commission, Manuals and Guides No. 56, UNESCO (English), 196 pp.

Jacobs, S., Giulivi, C., Dutrieux, P., Rignot, E., Nitsche, F., and Mouginot, J. (2013). Getz Ice Shelf melting response to changes in ocean forcing. *Journal of Geophysical Research: Oceans*, 118(June):4152–4168.

Jacobs, S. S. (1991). On the nature and significance of the Antarctic Slope Front. *Marine Chemistry*, 35(1-4):9–24.

Jacobs, S. S., Jenkins, A., Giulivi, C. F., and Dutrieux, P. (2011). Stronger ocean circulation and increased melting under Pine Island Glacier ice shelf. *Nature Geoscience*, 4(8):519–523.

Jacobs, S. S., Jenkins, A., Hellmer, H. H., Giulivi, C. F., Nitsche, F., Huber, B., and Guerrero, R. (2012). The Amundsen Sea and the Antarctic Ice Sheet. *Ocenaography*, 25(3):154–163.

Jenkins, A., Dutrieux, P., Jacobs, S. S., Mcphail, S. D., Perrett, J. R., Webb, A. T., and White, D. (2010). Observations beneath Pine Island Glacier in West Antarctica and implications for its retreat. *Nature Geoscience*, 3(July).

Kalén, O., Assmann, K. M., Wåhlin, A. K., Ha, H. K., Kim, T. W., and Lee, S. H. (2016). Is the oceanic heat flux on the central Amundsen sea shelf caused by barotropic or baroclinic currents? *Deep-Sea Research Part II: Topical Studies in Oceanography*, 123:7–15.

Kim, C. S., Kim, T. W., Cho, K. H., Ha, H. K., Lee, S. H., Kim, H. C., and Lee, J. H. (2016). Variability of the Antarctic Coastal Current in the Amundsen Sea. *Estuarine, Coastal and Shelf Science*, 181:123–133.

Lee, S. (2016). The Amundsen Sea Expedition 2015 2016. Technical Report February.

Lefebvre, W. and Goosse, H. (2005). Influence of the Southern Annular Mode on the sea ice-ocean system: The role of the thermal and mechanical forcing. *Ocean Science*, 1(3):145–157.

Lüpkes, C. and Birnbaum, G. (2005). Surface drag in the Arctic marginal sea-ice zone: A comparison of different parameterisation concepts. *Boundary-Layer Meteorology*, 117(2):179–211.

Martin, T., Tsamados, M., Schroeder, D., and Feltham, D. (2016). The impact of variable sea ice roughness on changes in Arctic Ocean surface stress: a model study. *Journal of Geophysical Research: Oceans*, 121(3):1931–1952.

McDougall, T. and Barker, P. (2011). *Getting started with TEOS-10 and the Gibbs Seawater (GSW) Oceanographic Toolbox*.

Mcintyre, T., Mcmahon, C. R., Muelbert, M. M. C., Nicholls, K., Picard, B., and Reverdin, G. (2017). Marine Mammals Exploring the Oceans Pole to Pole A Review of the MEOP Consortium. *Oceanography*, 30(2):132–138.

McLandress, C., Shepherd, T. G., Scinocca, J. F., Plummer, D. A., Sigmond, M., Jonsson, A. I., and Reader, M. C. (2011). Separating the dynamical effects of climate change and ozone depletion. Part II: Southern Hemisphere troposphere. *Journal of Climate*, 24(6):1850–1868.

Mo, K. C. (2000). Relationships between low-frequency variability in the Southern Hemisphere and sea surface temperature anomalies. *Journal of Climate*, 13(20):3599–3610.

Nakayama, Y., Timmermann, R., Schröder, M., and Hellmer, H. H. (2014). On the difficulty of modeling Circumpolar Deep Water intrusions onto the Amundsen Sea continental shelf. *OCEAN MODELLING*, 84(December 2014):26–34.

Nitsche, F. O., Jacobs, S. S., Larter, R. D., and Gohl, K. (2007). Bathymetry of the Amundsen Sea continental shelf: Implications for geology, oceanography, and glaciology. *Geochemistry, Geophysics, Geosystems*, 8(10):1–10.

NOAA (2019). Arctic / Antarctic Oscillation (AO/AAO), Retrieved from:. *https://www.cpc.ncep.noaa.gov/products/precip/CWlink/daily_ao_index/history/method.shtml#eof [Date accessed: 2019-09-29].*

NSIDC (2019). What are the EASE Grid. Retrieved from:. *https://nsidc.org/data/ease, [Date Accessed: 2019-09-29].*

Padman, L., Fricker, H. A., Coleman, R., Howard, S., and Erofeeva, L. (2002). A new tide model for the Antarctic ice shelves and seas. *Annals of Glaciology*, 34:247–254.

Padman, L., Siegfried, M. R., and Fricker, H. A. (2018). Ocean Tide Influences on the Antarctic and GreenlandIce Sheets. *Reviews of Geophysics*, 56(1):142–184.

Pawlowicz, R. (2019). M_map: A mapping package for MATLAB,version 1.4k, [Computer software], available online at www.eoas.ubc.ca/˜rich/map.html.

Pritchard, H. D., Ligtenberg, S. R. M., Fricker, H. A., Vaughan, D. G., Broeke, M. R. V. D., and Padman, L. (2012). Antarctic ice-sheet loss driven by basal melting of ice shelves. *Nature*, 484(April):502–505.

Raphael, M. N., Marshall, G. J., Turner, J., Fogt, R. L., Schneider, D., Dixon, D. A., Hosking, J. S., Jones, J. M., and Hobbs, W. R. (2016). The amundsen sea low: variability, change, and impact on Antarctic climate. *American Meteorological Society*, (January):111–122.

Rignot, E., Bamber, J., den Broeke, M., Davis, C. H., Li, Y., Berg, W. J., and van Meijgaard, E. (2008). Recent Antarctic ice mass loss from radar interferometry and regional climate modelling. *Nature Geoscience*, 1(January):106–110.

Rignot, E., Jacobs, S. S., Mouginot, J., and Scheuchl, B. (2013). Ice-shelf melting around Antarctica. *Science*, 341(6143):266–270.

Rignot, E., Mouginot, J., Scheuchl, B., Van Den Broeke, M., Van Wessem, M. J., and Morlighem, M. (2019). Four decades of Antarctic ice sheet mass balance from 19792017. *Proceedings of the National Academy of Sciences of the United States of America*, 116(4):1095–1103.

Schlosser, P., Bayer, R., Foldvik, A., Gammelsrød, T., Rohardt, G., and Munnich, K. O. (1990). 18 and Helium as Tracers of Ice Shelf Water and Water / Ice of the. *Journal of Geophysical Research*, 95(March):3253–3263.

Sciremammano, F. (1979). A suggestion for the presentation of correlations and their significance levels. *Notes and correspondence, American Meteorological Society*, (November):1273–1276.

Semper, S. and Darelius, E. (2017). Seasonal resonance of diurnal coastal trapped waves in the southern Weddel Sea, Antarctica. *Ocean Science*, 13(January):77–93.

Shepherd, A., Fricker, H. A., and Farrell, S. L. (2018). Trends and connections across the Antarctic cryosphere. *Nature*, 558(7709):223–232.

Spence, P., Griffies, S. M., England, M., McC. Hogg, A., Saenko, O. A., and Jourdain, N. C. (2014). Rapid subsurface warming and circulation changes of Antarctic coastal waters by poleward shifting winds. *Geophysical Research Letters*, 41(1):4601–4610.

Stammerjohn, S. E., Maksym, T., Massom, R. A., Lowry, K., Arrigo, K. R., Yuan, X., Raphael, M., Randall-Goodwin, E., Sherrell, R. M., and Yager, P. L. (2015). Seasonal sea ice changes in the amundsen sea, Antarctica, over the period of 1979-2014. *Elementa*, 3:1–20.

Stewart, A. L. and Thompson, A. F. (2015). Eddy-mediated transport of warm Circumpolar Deep Water across the Antarctic Shelf Break. *Geophysical*, 42(January):432–440.

Thoma, M., Jenkins, A., Holland, D., and Jacobs, S. (2008). Modelling Circumpolar Deep Water intrusions on the Amundsen Sea continental shelf, Antarctica. *Geophysical Research Letters*, 35(18):L18602.

Thompson, D. W. and Solomon, S. (2002). Interpretation of recent Southern Hemisphere climate change. *Science*, 296(5569):895–899.

Thompson, D. W., Solomon, S., Kushner, P. J., England, M. H., Grise, K. M., and Karoly, D. J. (2011). Signatures of the Antarctic ozone hole in Southern Hemisphere surface climate change. *Nature Geoscience*, 4(11):741–749.

Tschudi, M. A., Meier, W. N., and Stewart, J. S. (2019). An enhancement to sea ice motion and age products. *The Cryosphere Discussions*, (February):1–29.

Wåhlin, A. K., Kalén, O., Arneborg, L., Bjork, G., Carvajal, G. K., Ha, H. K., Kim, T. W., Lee, S. H., Lee, J. H., and Stranne, C. (2013). Variability of Warm Deep Water Inflow in a Submarine Trough on the Amundsen Sea Shelf. *Journal of Physical Oceanography*, 43(April):2054–2070.

Wåhlin, A. K., Muench, R. D., Arneborg, L., Björk, G., Ha, H. K., Lee, S. H., and Alsén, H. (2012). Some implications of ekman layer dynamics for cross-shelf exchange in the Amundsen sea. *Journal of Physical Oceanography*, 42(9):1461–1474.

Wåhlin, A. K., Yuan, X., Bjork, G., and Nohr, C. (2010). Inflow of Warm Circumpolar Deep Water in the Central Amundsen Shelf. *Journal of Physical Oceanography*, 40(February):1427–1434.

Walker, D. P., Jenkins, A., Assmann, K. M., Shoosmith, D. R., and Brandon, M. A. (2013). Oceanographic observations at the shelf break of the Amundsen Sea, Antarctica. *Journal of Geophysical Research: Oceans*, 118(6):2906–2918.

Yager, P. L., Sherrell, R. M., Stammerjohn, S. E., Alderkamp, A. C., Schofield, O., Abrahamsen, E. P., Arrigo, K. R., Bertilsson, S., Garay, D. L., Guerrero, R., Lowry, K. E., Moksnes, P. O., Ndungu, K., Post, A. F., Randall-Goodwin, E., Riemann, L., Severmann, S., Thatje, S., van Dijken, G. L., and Wilson, S. (2012). ASPIRE: The Amundsen sea Polynya international research expedition. *Oceanography*, 25(3):40–53.